https://doi.org/10.5194/egusphere-2026-2803
Preprint. Discussion started: 18 June 2026

Indirect cross-comparison of Landsat-9 and Copernicus Sentinel-2 using EMIT as a hyperspectral transfer reference

Francesco Bove[1,2] and Javier Gorroño[1]

[1]Research Institute of Water and Environmental Engineering (IIAMA), Universitat Politècnica de València, València, Spain
[2]Department of Electronics, Information and Bioengineering (DEIB), Politecnico di Milano, 20133 Milan, Italy

Correspondence: Javier Gorroño (jagorvie@upv.es)

Abstract.

Combining observations from multiple optical satellite missions is essential for building consistent, multi-decadal records of Earth's surface and atmosphere, but it requires that the participating sensors be radiometrically aligned. This study presents a global-scale, indirect cross-comparison of top-of-atmosphere (TOA) reflectance from Landsat-9 (L9) and the Copernicus Sentinel-2 (S2A and S2B) missions, using the hyperspectral imager EMIT (Earth Surface Mineral Dust Source Investigation) as a transfer reference. The Simultaneous Nadir Overpass (SNO) technique is first applied to each of the three sensor pairs—L9–S2, L9–EMIT, and S2–EMIT—and a double-differencing scheme then combines the L9–EMIT and S2–EMIT results into an indirect L9–S2 cross-comparison that no longer depends on EMIT's absolute calibration. The visible, near-infrared, and shortwave-infrared bands are compared using mean reflectance values within 1×1 km^2 areas to suppress measurement noise. The geometry of the matchups confirms the orbital constraints affecting direct L9–S2 comparisons: L9 systematically precedes S2 by approximately 14 minutes and the two sensors view the target from opposite sides of nadir. In contrast, the L9–EMIT and S2–EMIT matchups show no systematic bias in time difference or viewing geometry, owing to EMIT's non-Sun-synchronous orbit aboard the International Space Station. For each of the three direct cross-comparisons, the relative error remains within the combined measurement uncertainty for reflectance values above 0.2. The indirect L9–S2 comparison yields nearly constant biases (S2 minus L9) in the visible bands, with agreement better than 1% in the green and red bands and approximately -2.5% in the blue band. The near-infrared band agrees within 0.5% above a reflectance of 0.3 and shows a mild non-linear behaviour at lower reflectances. The shortwave-infrared bands display a similar trend with a positive bias of up to 2.5% at higher reflectances, consistent with the larger uncertainties of the L9–EMIT pair in this spectral region. Two features distinguish this methodology from a direct L9–S2 cross-comparison: EMIT's hyperspectral sampling removes the need for a spectral band adjustment factor, and its non-Sun-synchronous orbit eliminates the systematic angular and temporal mismatches that affect SNO comparisons between Sun-synchronous missions. The same scheme could be applied, with substantially smaller uncertainties, using forthcoming SI-traceable satellite (SITSat) missions as the transfer reference, providing simultaneous absolute calibration and cross-mission alignment.

https://doi.org/10.5194/egusphere-2026-2803
Preprint. Discussion started: 18 June 2026

1 Introduction

Optical satellite measurements have become a central tool for monitoring the changes affecting Earth's climate, surface, and atmosphere. Detecting trends from these observations requires consistent records spanning several decades, but the operational lifetime of any single mission is typically limited to a few years. The combined use of measurements from multiple sensors is therefore unavoidable, and it has the additional benefit of improving the effective revisit time, which is particularly valuable for capturing seasonal phenomena such as vegetation phenology (Pelletier et al., 2024) and for global land-cover characterisation (Xu et al., 2022). Several recent efforts go beyond ad-hoc combinations and produce harmonised datasets ready for operational use; a prominent example is the Harmonized Landsat and Sentinel-2 version 2.0 surface reflectance product (HLS v2), which merges observations from both missions into a seamless time series with improved temporal sampling (Ju et al., 2025).

Two of the missions most often combined in this way, and the focus of the present study, are the Copernicus Sentinel-2 (S2) constellation operated by ESA and the Landsat-9 (L9) mission operated by NASA and the U.S. Geological Survey. Sentinel-2 currently comprises the twin satellites S2A and S2B (and, more recently, S2C), each carrying the MultiSpectral Instrument (MSI) which acquires imagery in 13 spectral bands from the visible to the shortwave infrared at 10, 20, or 60 m spatial resolution. Landsat-9 carries the Operational Land Imager-2 (OLI-2), which acquires nine bands at 15 or 30 m resolution.

Combining measurements from different sensors requires that they refer to a common radiometric scale, ideally one that is traceable to the International System of Units (SI). In practice, this interoperability is achieved either by design—for example, by selecting closely matched spectral response functions—or a posteriori, by quantifying and correcting cross-sensor differences (Helder et al., 2018). Although optical instruments undergo extensive pre-launch characterisation, their response evolves on orbit because of changes in the operating environment and ageing of the optical and detector components, and they must therefore be re-calibrated regularly during the mission (Chander et al., 2009; Gascon et al., 2017; Levy et al., 2024). On-board calibration devices such as solar diffusers and internal lamps are the primary means of tracking these changes, but they introduce their own uncertainty contributions and are themselves subject to ageing.

Because the on-orbit knowledge provided by on-board calibration is imperfect, missions such as S2 and Landsat are routinely compared against external references. Two complementary strategies dominate the literature. The first is vicarious calibration over well-characterised ground targets: pseudo-invariant calibration sites (PICS) such as Libya 4, recommended by the Committee on Earth Observation Satellites (CEOS) for their high spatial homogeneity and temporal stability, are used to monitor long-term sensor stability and to derive empirical absolute calibration models (Mishra et al., 2014; Helder et al., 2013); ground-based reference networks such as the Radiometric Calibration Network (RadCalNet) provide automated top-of-atmosphere (TOA) reflectance estimates at a small number of instrumented sites, with a target uncertainty around 5% (Bouvet et al., 2019). The second strategy is cross-comparison between two orbiting sensors. In the so-called Simultaneous Nadir Overpass (SNO) approach, near-coincident acquisitions of the same scene by two missions are directly compared, taking advantage of the matched illumination, viewing, and atmospheric conditions to isolate the radiometric difference between the instruments (Chander et al., 2013a). In what follows we use *cross-comparison* to refer to the assessment of the relationship between two

https://doi.org/10.5194/egusphere-2026-2803
Preprint. Discussion started: 18 June 2026

sensors (for example through linear regression) and reserve *cross-calibration* for the subsequent application of that relationship as a correction.

Each of these strategies has well-known limitations. PICS-based comparisons are limited to a small number of bright, spectrally flat targets that do not represent the full dynamic range of typical Earth scenes, and they require a Bidirectional Reflectance Distribution Function (BRDF) model to handle off-nadir or non-coincident acquisitions. RadCalNet sites are spatially restricted and suffer from infrequent sensor overpasses, BRDF correction needs, and site maintenance (Bouvet et al., 2019). Direct SNO cross-comparisons between S2 and Landsat are constrained by the geometry of their respective Sun-synchronous orbits: the two missions follow different repeat cycles, so truly coincident overpasses are rare and confined to a small fraction of the Earth's surface, and at the remaining locations the two sensors typically view the target from opposite sides of the nadir (i.e. opposite azimuth angle values) with a time difference of several minutes (Helder et al., 2018). Any residual spectral mismatch between the corresponding bands must additionally be corrected through a Spectral Band Adjustment Factor (SBAF) derived from a hyperspectral reference (Zhang et al., 2018). The SBAF itself is target-dependent and contributes additional uncertainty to the comparison (Chander et al., 2013b; Pinto et al., 2016; Farhad et al., 2020).

A way to relax several of these constraints is to introduce a hyperspectral imager as an intermediate transfer reference between the two multispectral sensors. The high spectral sampling of a hyperspectral instrument allows each multispectral band to be reconstructed by spectral convolution, removing the need for an a-priori SBAF. If, in addition, the hyperspectral mission has an orbit that is not Sun-synchronous, the resulting matchups between the reference and each multispectral sensor cover a wider and more symmetric range of viewing geometries and time differences, reducing the systematic biases that affect direct S2–L9 cross-comparisons (Gorroño et al., 2024).

In this paper we adopt this strategy and use the Earth Surface Mineral Dust Source Investigation (EMIT) mission as a hyperspectral transfer reference between L9 and S2. EMIT was developed at NASA's Jet Propulsion Laboratory and has been operating from the International Space Station (ISS) since 14 July 2022 (Green et al., 2020). Its imaging spectrometer covers the 380–2500 nm range with approximately 7.5 nm spectral sampling and 60 m spatial resolution, and on-orbit characterisation by the EMIT team has demonstrated excellent radiometric performance, with surface-reflectance accuracy assessed against in-situ measurements at the percent level (Thompson et al., 2024; Coleman et al., 2024). EMIT is mounted on the ISS, whose precessing, non-Sun-synchronous orbit produces a varied sampling of solar and viewing geometries that is well suited to a transfer-reference role.

The objective of this work is to perform an indirect cross-comparison of L9 and S2 TOA reflectance using EMIT as a hyperspectral anchor. We first apply the SNO technique to each of the three sensor pairs (L9–S2, L9–EMIT, S2–EMIT), and then combine the L9–EMIT and S2–EMIT comparisons through a double-differencing scheme (Chander et al., 2013a) that cancels the contribution of the reference and yields an indirect L9–S2 comparison free of SBAF corrections. The proposed methodology offers two advantages over a direct L9–S2 comparison: it removes the need for spectral band adjustment, and it uses an intermediate sensor whose orbit produces a more balanced angular and temporal mismatch with each of the multispectral missions. The methodology is general and could be applied, with even higher accuracy, to proposed SI-traceable satellite

https://doi.org/10.5194/egusphere-2026-2803
Preprint. Discussion started: 18 June 2026

(SITSat) missions such as TRUTHS (Fox and Green, 2020) and CLARREO Pathfinder (Roithmayr et al., 2014), which are explicitly designed to serve as on-orbit calibration references for the existing fleet of optical sensors.

The remainder of the paper is organised as follows. Section 2 describes the data products, the construction of the matchup ensembles, and the cross-comparison techniques used. Section 3 presents the cardinality of the resulting ensembles, the distributions of time and angular differences across the three sensor pairs, the TOA reflectance scatter plots and calibration curves, and the relative-error assessment for both the direct and the indirect comparisons. The findings and their implications for L9–S2 interoperability, together with the limitations of the present study and prospects offered by future SITSat references, are discussed in the final section.

2 Methodology

2.1 Cross-comparison techniques

This study exploits two complementary cross-comparison techniques. The first is the Simultaneous Nadir Overpass (SNO) approach (Chander et al., 2013a), in which two sensors S_1 and S_2 acquire the same Area Of Interest (AOI) of the Earth's surface within a short time window and with similar viewing and illumination geometries, so that their measurements can be related directly. Throughout the paper the relationship between S_1 and S_2 over the resulting ensemble of matchups is summarised through a linear regression of the form

$$\rho_{S_2}^{TOA} = a_{S_1,S_2}\,\rho_{S_1}^{TOA} + b_{S_1,S_2}, \tag{1}$$

where ρ^{TOA} denotes top-of-atmosphere (TOA) reflectance and $(a_{S_1,S_2}, b_{S_1,S_2})$ are the slope and intercept obtained from the matchup ensemble.

The second technique is the double-differencing method, in which S_1 and S_2 are compared *indirectly* through an intermediate sensor S_{int} that acts as a transfer reference. The two direct relationships S_1–S_{int} and S_2–S_{int} are combined so as to cancel the contribution of S_{int}, yielding an estimate of the S_1–S_2 difference that no longer depends on the absolute calibration of the reference. The indirect comparison can be written as

$$\Delta\rho_{S_1,S_2}^{TOA} = \Delta\rho_{S_1,S_{int}}^{TOA} - \Delta\rho_{S_2,S_{int}}^{TOA}, \tag{2}$$

where $\Delta\rho_{S_i,S_j}^{TOA}$ denotes the radiometric difference between S_i and S_j inferred from the corresponding linear regression (Eq. (1)). The underlying assumption, as discussed by Chander et al. (2013a), is that the response of S_{int} is sufficiently stable over the range of conditions sampled by the two direct comparisons.

In the present study the SNO technique is applied to each of the three sensor pairs: L9 vs S2 (S_1 = Landsat-9, S_2 = Sentinel-2), L9 vs EMIT (S_1 = Landsat-9, S_2 = EMIT) and S2 vs EMIT (S_1 = Sentinel-2, S_2 = EMIT). The L9–EMIT and S2–EMIT regressions are then combined through Eq. (2) to obtain an indirect L9–S2 cross-comparison, with EMIT playing the role of S_{int}.

https://doi.org/10.5194/egusphere-2026-2803
Preprint. Discussion started: 18 June 2026

The interpretation of the resulting biases requires a reference scale, which we take to be the radiometric measurement uncertainty of each instrument, understood as the dispersion of values that can reasonably be attributed to the measurand (JCGM, 2008). Because each comparison aggregates many pixels, spatiotemporally uncorrelated contributions such as detector noise are negligible at this scale and are not considered. For the OLI on Landsat-8, Markham et al. (2014) reported an on-orbit calibration performance better than 3%, and Gascon et al. (2017) reported a similar 3% figure for the MSI on Sentinel-2A. We adopt 3% as the reference radiometric uncertainty for Landsat-9, Sentinel-2A and Sentinel-2B, on the basis of the strong heritage of OLI-2 with respect to OLI and of MSI-B with respect to MSI-A. For EMIT we adopt 5%, consistent with the agreement reported between EMIT and RadCalNet across most of its spectral channels in the U.S. Geological Survey assessment (Shrestha et al., 2024).

2.2 Data products

The physical quantity used for the cross-comparison is the TOA reflectance. Level-1 products are used throughout the analysis, so that no atmospheric correction enters the processing chain. All satellite data are accessed and processed through the Google Earth Engine (GEE) platform, which couples a multi-petabyte catalogue of satellite imagery and geospatial datasets with planetary-scale analysis capabilities; the Python API is used to script the analysis (Gorelick et al., 2017).

In GEE, the Level-1 products of the three missions are not delivered in an identical form. For Landsat-9, the catalogue provides calibrated TOA reflectance for OLI-2; for Sentinel-2, it provides the Level-1C orthorectified TOA reflectance product; and for EMIT, it provides the Level-1B at-sensor calibrated radiance. The corresponding GEE image collections used in this work are

- Landsat-9: `ee.ImageCollection("LANDSAT/LC09/C02/T1_TOA")`;
- Sentinel-2: `ee.ImageCollection("COPERNICUS/S2_HARMONIZED")`;
- EMIT: `ee.ImageCollection("NASA/EMIT/L1B/RAD")`.

The L9 and S2 collections can be used directly in the cross-comparison, whereas the EMIT radiance product must be (i) spectrally convolved onto the OLI-2 and MSI spectral response functions to obtain band-equivalent multispectral measurements, and (ii) converted to TOA reflectance. Both operations are described in Section 2.3.4.

The SNO technique relies on the assumption that the spectral content of the two sensors being compared is similar. Accordingly, the L9 and S2 bands are matched pairwise as is standard in the Landsat-Sentinel cross-calibration literature; the six band pairs used in this study, together with the corresponding central wavelength λ_c, bandwidth (BW) and spatial resolution, are listed in Table 1. Figure 1 shows the SRFs of OLI-2 and of the two MSI units flown on S2A and S2B; both S2A and S2B acquisitions are used in the analysis, and the small differences between the two MSI SRFs are propagated explicitly through the EMIT spectral convolution (Section 2.3.4).

https://doi.org/10.5194/egusphere-2026-2803
Preprint. Discussion started: 18 June 2026

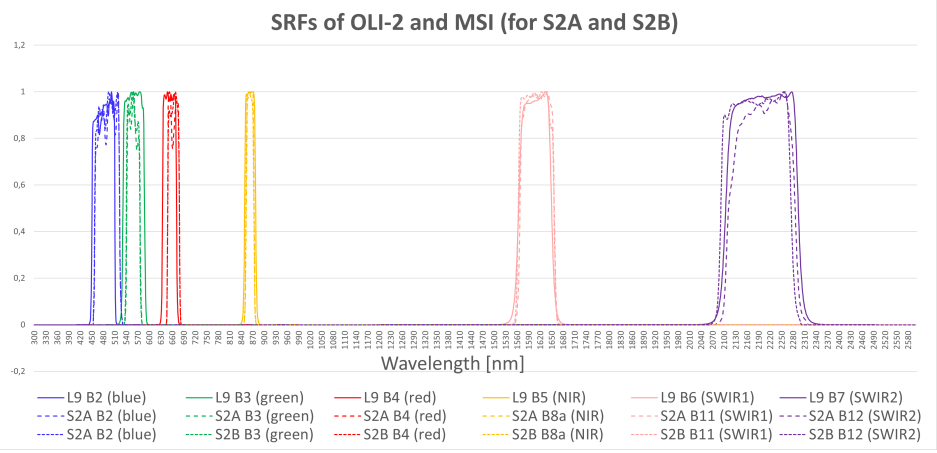

Figure 1. Spectral Response Functions (SRFs) of OLI-2 and of the MSI units flown on Sentinel-2A and Sentinel-2B.

	Landsat-9				**Sentinel-2**					
Spectral portion	**Band**	λ_c (nm)	BW (nm)	Resolution (m)	**Band**	λ_c^{S2A} (nm)	BW^{S2A} (nm)	λ_c^{S2B} (nm)	BW^{S2B} (nm)	Resolution (m)
Blue	B2	482	65	30	B2	492.7	64	492.3	65	10
Green	B3	562	75	30	B3	559.8	35	558.9	35	10
Red	B4	655	50	30	B4	664.6	30	664.9	31	10
NIR	B5	865	40	30	B8a	832.8	118	832.9	115	10
SWIR 1	B6	1610	100	30	B11	1613.7	88	1610.4	93	20
SWIR 2	B7	2200	200	30	B12	2202.4	179	2185.7	181	20

Table 1. Landsat-9 and Sentinel-2 spectral characteristics (for both S2A and S2B)

2.3 Construction of the matchup ensembles

The SNO technique requires pairs of acquisitions of the same target with a small time difference and similar viewing geometry. We refer to each such pair as a *matchup* and define it as two satellite images of the same Area Of Interest (AOI), acquired within a maximum time difference Δt_{max}^{acq}. The collection of all matchups retained for a given sensor pair is the *matchup ensemble*, denoted M_{S_1,S_2}.

The construction of the three matchup ensembles ($M_{L9,S2}$, $M_{L9,EMIT}$ and $M_{S2,EMIT}$) is carried out independently for each sensor pair and proceeds in five steps: (i) definition of the spatial and temporal bounds of the search and identification of overlapping acquisitions (Section 2.3.1); (ii) assignment of a per-image cloud score (Section 2.3.2); (iii) assignment of the illumination and viewing angles to each matchup (Section 2.3.3); (iv) extraction of the per-band TOA reflectance values within the matchup AOI (Section 2.3.4); and (v) filtering of the resulting ensembles against a common set of radiometric,

https://doi.org/10.5194/egusphere-2026-2803
Preprint. Discussion started: 18 June 2026

geometric and scene-homogeneity criteria (Section 2.3.6). For the direct L9 vs S2 cross-comparison an additional Spectral Band Adjustment Factor (SBAF) correction is applied to the MSI reflectance, as described in Section 2.3.7.

2.3.1 Matchup bounds and geometry

The three matchup ensembles are built by querying the GEE archive for image pairs that satisfy a common set of bounds. The bounds are a compromise between ensemble cardinality and computational cost, and were set as follows:

- acquisitions from the year 2024 only;
- latitude in the range $[-60°, +60°]$, which contains the EMIT coverage limits and a comfortable margin for the other two missions;
- maximum time difference between the two acquisitions $\Delta t^{acq}_{max} = 15$ minutes;
- candidate AOIs of $1° \times 1°$ in latitude/longitude (approximately 100×100 km at the equator).

To simplify the search, the Earth is tiled along the latitude/longitude grid so that the candidate AOIs are axis-aligned. Within each $1° \times 1°$ tile the matchup conditions are evaluated separately for each cross-comparison pair, producing a preliminary list of overlapping acquisitions. Because two acquisitions in a tile typically overlap only partially, each candidate AOI is then subdivided into a 100×100 grid of cells of $0.01° \times 0.01°$ (approximately 1×1 km). Only the cells in which both acquisitions are fully valid and spatially overlap across all of their pixels are retained. The resulting matchups are therefore 1×1 km AOIs filled with two valid and fully overlapping satellite images, one from each mission in the pair.

2.3.2 Cloud score computation

Cloud contamination must be excluded from the matchup ensembles. To this end, a *cloud score* is computed for each acquisition; the procedure differs between missions:

- For Landsat-9, GEE provides the `QA_PIXEL` band at 30 m resolution, a 16-bit quality assessment band co-registered with the Level-1 scene. From `QA_PIXEL` we extract bit 6, the Clear flag, which is set to 0 when either the Cloud or the Dilated Cloud bit is active and to 1 otherwise. The L9 cloud score is the fraction of 30×30 m pixels within the AOI for which the Clear flag is 0, i.e. the percentage of cloudy pixels.
- For Sentinel-2, GEE provides a dedicated 10 m cloud-probability product, available in the image collection

  `ee.ImageCollection("COPERNICUS/S2_CLOUD_PROBABILITY")`.

  The S2 cloud score is the mean of these per-pixel probabilities within the AOI.
- For EMIT L1B, GEE does not deliver an auxiliary cloud-quality band. At this stage the cloud score associated with an L9–EMIT or S2–EMIT matchup is therefore the one derived from the L9 or S2 image of the pair. The EMIT acquisition

https://doi.org/10.5194/egusphere-2026-2803
Preprint. Discussion started: 18 June 2026

itself is further screened later, at the filtering stage, by means of its reflectance in the cirrus band derived from the spectral convolution (Section 2.3.4).

2.3.3 Illumination and viewing angles

The radiance recorded at the sensor depends on the solar and viewing geometry, so a representative Solar Zenith Angle (SZA), Viewing Zenith Angle (VZA) and Viewing Azimuth Angle (VAA) are assigned to each acquisition in every matchup. For Landsat-9 and EMIT, GEE delivers these angles as per-pixel bands, and we use their mean over the 1×1 km AOI. For Sentinel-2, GEE delivers only a single average value per scene (covering approximately 110×110 km), which is too coarse for the present analysis. The full angular grids are therefore retrieved from the Amazon S3 mirror of the Sentinel-2 archive (Sinergise and Amazon Web Services, 2024), where they are stored as XML metadata accompanying each granule. The metadata provide SZA, VZA and VAA values on a 5 km grid. The matrix is resampled to a per-pixel grid using a 2D spline interpolation with a step of $0.01^\circ/2$, and the angles associated with each S2 acquisition are taken from the interpolated value at the centre of the 1×1 km AOI.

2.3.4 Radiometric values extraction

For each matchup, TOA reflectance is extracted from both acquisitions. The value associated with a given image and band is the mean of the TOA reflectance pixel values inside the 1×1 km AOI, denoted $\rho_{S_1}^{TOA}$ and $\rho_{S_2}^{TOA}$; the corresponding standard deviations $\sigma_{S_1}^{AOI}$ and $\sigma_{S_2}^{AOI}$ are also retained for use in the filtering and uncertainty analyses. Border pixels that are only partially contained in the AOI are included as full pixels; the resulting second-order effect on the AOI-mean reflectance is negligible compared with the radiometric quantities of interest. Reflectances are extracted for the six spectral bands listed in Table 1 and, in addition, for the *cirrus band* of each multispectral mission (B9 for Landsat-9, B10 for Sentinel-2), which is used in the filtering step (Section 2.3.6).

For the L9 vs S2 cross-comparison the TOA reflectance is taken directly from the GEE Level-1 products, and the AOI mean and standard deviation are computed on the native grids of the two missions.

For the comparisons that involve EMIT, GEE delivers at-sensor radiance over the 256 EMIT channels (spectral sampling of approximately 7.5 nm), which must be (i) spectrally convolved onto the OLI-2 or MSI band of interest and (ii) converted to TOA reflectance. The convolution follows the procedure of Gorroño et al. (2017). For each AOI, the EMIT radiance spectrum is linearly interpolated onto a 1 nm grid to produce a simulated at-sensor radiance profile $L_{atm}(\lambda)$. The target SRF, $\mathrm{SRF}_{S_1}(\lambda)$, of the OLI-2 or MSI band under consideration (distinguishing between S2A and S2B for the MSI case) is interpolated onto the same grid by cubic-spline interpolation, and the band-equivalent EMIT radiance is obtained as a weighted average,

$$L_{EMIT} = \frac{\sum_\lambda \mathrm{SRF}_{S_1}(\lambda)\, L_{atm}(\lambda)}{\sum_\lambda \mathrm{SRF}_{S_1}(\lambda)}, \tag{3}$$

where S_1 denotes the multispectral mission against which EMIT is being compared. L_{EMIT} can be interpreted as the radiance that the OLI-2 or MSI sensor would have measured under the same atmospheric and surface conditions sampled by EMIT.

https://doi.org/10.5194/egusphere-2026-2803
Preprint. Discussion started: 18 June 2026

The conversion of L_{EMIT} to TOA reflectance follows the standard expression

$$\rho^{TOA}_{EMIT} = \frac{\pi\, L_{EMIT}}{\cos(\mathrm{SZA}_{EMIT})\, k}, \tag{4}$$

where the scaling factor k collects the band-integrated extraterrestrial solar irradiance and the Sun-Earth distance correction. Rather than computing k from a solar irradiance model in absolute terms, we infer it from the multispectral mission itself by inverting Eq. (4) applied to the radiance and reflectance of S_1:

$$k = \frac{\pi\, L_{S_1}}{\cos(\mathrm{SZA}_{S_1})\, \rho^{TOA}_{S_1}}. \tag{5}$$

The role of k defined in this way is operational rather than radiometric: it ensures that the EMIT reflectance entering each direct comparison is computed under the same Sun-Earth distance, the same illumination geometry and the same band convolution that are implicit in the corresponding multispectral reflectance. Using Eqs. (4) and (5), the EMIT reflectance can be written explicitly as

$$\rho^{TOA}_{EMIT} = \rho^{TOA}_{S_1} \left(\frac{L_{EMIT}}{L_{S_1}} \right) \left(\frac{\cos(\mathrm{SZA}_{S_1})}{\cos(\mathrm{SZA}_{EMIT})} \right), \tag{6}$$

which makes this geometric and spectral matching apparent. The same expression is applied to the AOI standard deviation σ^{AOI}_{EMIT}.

The radiance L_{S_1} that appears in Eqs. (5) and (6) is obtained from the multispectral product as follows. For Landsat-9, the conversion from the Level-1 product is performed with the GEE function

`ee.Algorithms.Landsat.calibratedRadiance()`,

which takes as input the raw Level-1 scenes (`"LANDSAT/LC09/C02/T1"`) and converts digital numbers to at-sensor radiance following the standard linear calibration (Chander et al., 2009), with sensor-specific gain and bias coefficients read from the scene metadata. For Sentinel-2, GEE does not provide a dedicated radiance product, but the per-image metadata contain the coefficients required for the conversion. The at-sensor radiance is recovered from the reflectance product as

$$L_{S2} = \frac{\rho^{TOA}_{S2} \cos(\mathrm{SZA}_{S2})\, E_{Sun}\, U}{\pi}, \tag{7}$$

where E_{Sun} is the band-integrated solar irradiance and U is the Sun-Earth distance correction factor.

2.3.5 Solar irradiance model.

The two multispectral missions adopt different solar irradiance models in their Level-1 processing: the Chance and Kurucz model for Landsat-9 (Chance and Kurucz, 2010) and the Thuillier model for Sentinel-2 (Thuillier et al., 2003). In the multispectral processing, the irradiance model is used twice — at the radiometric calibration of radiance and again at the radiance-to-reflectance conversion — and its contribution therefore cancels at the reflectance level. The L9 and S2 TOA reflectances entering the cross-comparison are consequently insensitive to the choice of irradiance model.

https://doi.org/10.5194/egusphere-2026-2803
Preprint. Discussion started: 18 June 2026

Band	ChuKur[W/m^2 sr m] ($k^{\mathrm{Bx}}_{Sentinel-2}$)	Thuillier[W/m^2 sr m] ($k^{\mathrm{Bx}}_{Landsat-9}$)
Blue	495.43	502.83
Green	466.35	458.55
Red	396.24	391.13
NIR	240.42	240.73
SWIR1	62.15	63.48
SWIR2	20.44	21.18

Table 2. E-Sun model computed panel radiance for the Chance and Kurucz model model used for Landsat (Chance and Kurucz, 2010) and the Thuillier model used for the MSI measurements (Thuillier et al., 2003)

The EMIT reflectance, by contrast, is computed via Eq. (4), where the irradiance model enters only once. Because k is inferred from the multispectral mission through Eq. (5), the EMIT reflectance in each direct comparison inherits the irradiance model of the multispectral mission it is being compared with: Chance and Kurucz in the L9–EMIT branch and Thuillier in the S2–EMIT branch. Each of the two direct comparisons therefore carries a residual sensitivity to the irradiance model on the EMIT side; this residual is a known limitation of the direct approach.

In the indirect L9–S2 comparison obtained through Eq. (2), the EMIT contribution cancels in the double difference, but only if the L9–EMIT and S2–EMIT branches use the same irradiance convention for EMIT. The two direct branches as built do not, since each was processed with the model of its respective multispectral mission. The two are aligned a posteriori by rescaling the EMIT reflectance of the S2–EMIT branch onto the Chance and Kurucz convention used by the L9–EMIT branch. Denoting by $k^{B_x}_{L9}$ and $k^{B_x}_{S2}$ the band-integrated solar contributions associated with the Chance and Kurucz and the Thuillier models for band B_x, the corrected EMIT reflectance entering the S2–EMIT comparison used in the double difference is

$$\rho^{TOA,B_x}_{EMIT,\mathrm{corr}} = \frac{k^{B_x}_{S2}}{k^{B_x}_{L9}}\,\rho^{TOA,B_x}_{EMIT}, \tag{8}$$

where the $k^{B_x}_{L9}$ and $k^{B_x}_{S2}$ values are taken from Levy et al. (2024) and reported in Table 2. The Chance and Kurucz convention is taken as the common reference for convenience; any common convention — or no irradiance model at all — would be equivalent for the indirect comparison once the two branches are aligned, since the EMIT contribution then cancels exactly in the double difference. The same rescaling is applied to σ^{AOI}_{EMIT}. The irradiance-model residual that affects the two direct branches is thus removed in the indirect L9–S2 comparison, which is the primary deliverable of this work.

2.3.6 Ensemble filtering

At this point each matchup in a generic ensemble M_{S_1,S_2} is fully characterised by:

- the two satellite images from missions S_1 and S_2;

https://doi.org/10.5194/egusphere-2026-2803
Preprint. Discussion started: 18 June 2026

- the AOI location and the acquisition date of each image;
- the time difference of acquisition between the two images;
- the cloud score of each image;
- the per-image illumination and viewing angles SZA_{S_i}, VZA_{S_i} and VAA_{S_i} $(i = 1, 2)$;
- the AOI-mean TOA reflectance $\rho_{S_i}^{TOA}$ and its standard deviation $\sigma_{S_i}^{AOI}$ for each spectral band considered, including the cirrus band.

A reliable cross-comparison requires that residual contributions unrelated to the radiometric response of the two sensors be suppressed. Each ensemble M_{S_1,S_2} is therefore filtered against a common set of geometric, radiometric and scene-homogeneity criteria, which we describe below; the resulting numerical thresholds are summarised in Table 3.

Illumination and viewing geometry. The maximum SZA is set to $60°$ in all three pairs, to avoid acquisitions strongly affected by atmospheric path length. For the viewing geometry the three missions do not behave equivalently: Landsat-9 and Sentinel-2 routinely acquire near-nadir scenes, while EMIT, mounted on the ISS, typically views at $5°$–$10°$ off-nadir (Roger et al., 2025). For the direct L9 vs S2 comparison we therefore require $\mathrm{VZA} < 5°$ for both sensors since it will maximise BRDF symmetry and largely skips hot-spot effects (Gorroño et al., 2024). For the comparisons that include EMIT, we require the absolute difference of the viewing zenith angles to be smaller than $5°$, $|\mathrm{VZA}_{S_1} - \mathrm{VZA}_{EMIT}| < 5°$, together with VAA in the $[20°, 160°]$ range to reduce azimuthal differences with S2 and Landsat (for $\mathrm{VAA} > 5°$, their VAA are within this range).

Cloud screening. The cloud score (Section 2.3.2) is required to be below 5%. To screen residual cirrus contamination, the AOI-mean TOA reflectance in the cirrus band (B9 for Landsat-9 and B10 for Sentinel-2), which is centred around 1375 nm where the atmosphere is strongly absorbing and cirrus clouds appear bright (Coluzzi et al., 2018), is required to be below 0.005.

Scene type. The cross-comparison is restricted to land surfaces excluding dense vegetation and dense urban environments. Water bodies and densely vegetated targets are excluded by requiring the Normalized Difference Vegetation Index (NDVI), computed from the red and NIR AOI-mean reflectances, to lie in $[0, 0.2]$. The remaining AOI is required to be moderately bright and homogeneous: the AOI-mean reflectance is required to lie between 0.1 and the 95th percentile P_{95} of its distribution, and the relative AOI standard deviation,

$$\sigma_{rel}^{AOI} = \frac{\sigma^{AOI}}{\rho^{TOA}}, \tag{9}$$

is required to lie below the 50th percentile P_{50} of its distribution. The P_{50} threshold is applied independently per spectral band and per mission in the pair, so that the homogeneity criterion is enforced consistently in both acquisitions and in every band used in the cross-comparison.

The resulting filtered ensembles for the three sensor pairs are those used in Section 3.

https://doi.org/10.5194/egusphere-2026-2803
Preprint. Discussion started: 18 June 2026

Filtering parameter	L9 vs S2	L9 vs EMIT	S2 vs EMIT
Cloud score	< 5%		
ρ^{TOA}_{cirrus}	< 0.005		
SZA	< 60 °		
NDVI range	[0, 0.2]		
Relative standard deviation (σ^{AOI}_{rel})	< P_{50}		
Reflectance range	[0.1, P_{95}]		
VZA	< 5 °	/	/
VZA^{abs}_{diff}	/	< 5 °	
VAA	/	[20°, 160°]	

Table 3. Matchup ensembles filtering parameters

2.3.7 Spectral Band Adjustment Factor for the direct L9 vs S2 comparison

The direct L9 vs S2 cross-comparison is subject to the residual spectral mismatch between the corresponding OLI-2 and MSI bands, which must be corrected through a Spectral Band Adjustment Factor (SBAF). We adopt the SBAF coefficients reported by Zhang et al. (2018). These coefficients were derived from a Landsat-8/Sentinel-2A comparison, but OLI-2 is the direct heritage of OLI and the MSI on Sentinel-2B is nominally identical to the MSI on Sentinel-2A; the small residual differences in the SRFs are absorbed in the dispersion of the comparison. Among the SBAF coefficients available in the literature, these are, to the best of our knowledge, the only ones derived directly on TOA reflectance and considering multiple surface types, both of which are relevant for the present analysis.

The MSI reflectance of band B_x is corrected as

$$\rho^{TOA,\text{corr}}_{B_x,S2} = m^{B_x}_{corr}\,\rho^{TOA}_{B_x,S2} + q^{B_x}_{corr}, \tag{10}$$

with the slope $m^{B_x}_{corr}$ and intercept $q^{B_x}_{corr}$ taken from Zhang et al. (2018) and reported in Table 4. The corrected reflectance $\rho^{TOA,\text{corr}}_{B_x,S2}$ is the quantity entered in the direct L9 vs S2 regression. The L9–EMIT and S2–EMIT comparisons do not require any SBAF, since the EMIT hyperspectral spectrum is convolved onto the target band through Eq. (3).

3 Results

3.1 Matchup ensembles cardinality and locations

The cardinalities of the three matchup ensembles, after application of the filters described in Section 2.3.6, are reported in Table 5, with the L9 vs S2 and S2 vs EMIT pairs further split between S2A and S2B. Three features of the table are worth noting. First, the number of matchups varies systematically between the three sensor pairs: the L9 vs S2 ensemble is the largest, the S2 vs EMIT ensemble is intermediate, and the L9 vs EMIT ensemble is the smallest. This ordering reflects the

https://doi.org/10.5194/egusphere-2026-2803
Preprint. Discussion started: 18 June 2026

Band	m_{corr}	q_{corr}
Blue	0.8729	0.0154
Green	0.9621	0.0027
Red	0.9103	0.0066
NIR	0.9701	0.0056
SWIR1	0.9668	0.0019
SWIR2	0.9702	0.0005

Table 4. Correction factors applied to the MSI reflectance measurements, for the the Landsat-9 vs Sentinel-2 cross-comparison case, for the six bands considered.

Band	**L9 vs S2**			**L9 vs EMIT**	**S2 vs EMIT**		
	S2A	**S2B**	**Total**	**Total**	**S2A**	**S2B**	**Total**
Blue	77 840	87 488	165 328	33 758	49 737	39 093	88 830
Green	84 990	91 343	176 333	39 133	50 322	38 444	88 766
Red	112 204	114 664	226 868	45 812	57 991	41 471	99 462
NIR	111 262	106 054	217 316	38 992	50 759	34 861	85 620
SWIR1	119 210	121 624	240 834	44 861	52 941	36 344	89 285
SWIR2	130 379	129 615	259 994	50 469	57 518	40 645	98 163

Table 5. Number of matchups for the different bands and for each cross-comparison case

underlying orbital geometries and revisit cycles: L9 and S2 share near-identical Sun-synchronous orbits and produce many quasi-coincident acquisitions, whereas the matchups with EMIT depend on intersections between the ISS orbit and the polar orbits of L9 and S2. The smaller size of the L9 vs EMIT ensemble relative to S2 vs EMIT follows directly from the longer L9 revisit time (16 days, against 5 days for the combined S2A/S2B constellation). Second, within each pair the number of matchups grows from the blue to the SWIR2 band. This is driven by the per-band reflectance filter (Section 2.3.6), which retains AOIs with mean reflectance above 0.1: bright targets satisfy this threshold more frequently in the longer wavelengths than in the visible, leading to progressively larger ensembles toward the SWIR. Third, even after filtering all ensembles remain of the order of tens of thousands of matchups of 1×1 km, which is sufficient to suppress measurement noise and ensure the statistical robustness of the regressions presented in Section 3.3.

The geographic distribution of the matchup locations is shown for the NIR band in Figure 2: panel (a) for L9 vs S2, panel (b) for L9 vs EMIT, and panel (c) for S2 vs EMIT. The L9 vs S2 matchups appear as a regular striped pattern dictated by the overlap of two near-identical Sun-synchronous repeat cycles, which produces matchups at well-defined longitudes and repeating with the orbital periodicity. By contrast, the comparisons that involve EMIT distribute the matchups much more uniformly across the globe, owing to the precessing, non-Sun-synchronous orbit of the ISS that randomises the longitudes at which overpasses

https://doi.org/10.5194/egusphere-2026-2803
Preprint. Discussion started: 18 June 2026

become near-coincident with the L9 and S2 acquisitions. In all three cases the matchups concentrate over the low-cloud, low-vegetation regions admitted by the filtering (Section 2.3.6)—primarily arid and semi-arid land surfaces in northern Africa, the Middle East, central Asia, Australia, and parts of the Americas—while remaining distributed across at least 30 spatially distinct areas. The EMIT-based ensembles are confined to latitudes within roughly $\pm 52^{\circ}$ as imposed by the ISS orbit inclination.

3.2 Ensembles distribution of different features

3.2.1 Time difference of acquisition distribution results

We now turn to the distributions of the matchup features (time difference of acquisition and viewing/illumination angles) across the three sensor pairs, which are essential to interpret the cross-comparisons that follow. The time difference of acquisition is defined, for each matchup, as

$$\Delta t^{acq}_{S_1,S_2} = t^{acq}_{S_1} - t^{acq}_{S_2}, \tag{11}$$

and is bounded by construction to $|\Delta t^{acq}_{S_1,S_2}| \leq 15$ minutes (Section 2.3.1). Table 6 reports the minimum, maximum, mean, and standard deviation of $\Delta t^{acq}_{S_1,S_2}$ for each band and cross-comparison case.

The L9 vs S2 distributions are systematically biased toward negative values, with a mean of approximately -14 minutes and a standard deviation below one minute across all bands. The convention of Eq. (11) therefore indicates that Landsat-9 consistently precedes Sentinel-2 over the matchup AOIs. This bias is consistent with the difference in the mean local solar time at the descending (daylight) node of the two Sun-synchronous orbits: 10:00 a.m. (± 15 min) for L9 (Masek et al., 2020) and 10:30 a.m. for S2 (Drusch et al., 2012). The two crossing times differ nominally by 30 minutes; the observed mean (~ 14 min) is smaller in magnitude because the matchups are not coincident overpasses of the same orbital phase but pairs of acquisitions selected from the two missions whose distinct repeat cycles (16 days for L9, 5 days for the combined S2 constellation) happen to bring their swaths over a common AOI within the ± 15 min temporal window imposed by the matchup filtering. The observed mean is therefore the statistic of this filtered population rather than a direct projection of the 30-minute LMT offset, and its sub-minute standard deviation reflects the near-deterministic character of the relative Sun-synchronous geometry once the matchup window is fixed.

The cross-comparisons that involve EMIT show a markedly different behaviour. The mean of $\Delta t^{acq}_{L9,EMIT}$ is approximately $+3$ minutes and that of $\Delta t^{acq}_{S2,EMIT}$ is essentially zero, with standard deviations of 7–8 minutes covering the entire ± 15 min window. The distributions are therefore approximately symmetric around zero and effectively unbiased with respect to acquisition time. This is a direct consequence of the precessing, non-Sun-synchronous ISS orbit: the time at which EMIT acquires a given target is decoupled from the fixed local times of the L9 and S2 acquisitions, so that the matchups sample the entire admissible time window. The small residual mean of the L9 vs EMIT case (only a few minutes) is statistical fluctuation given the much smaller ensemble size compared with the L9 vs S2 pair (Table 5). The qualitative behaviour described above is clearly visible in the corresponding histograms shown in Figure 3 for the NIR band.

https://doi.org/10.5194/egusphere-2026-2803
Preprint. Discussion started: 18 June 2026

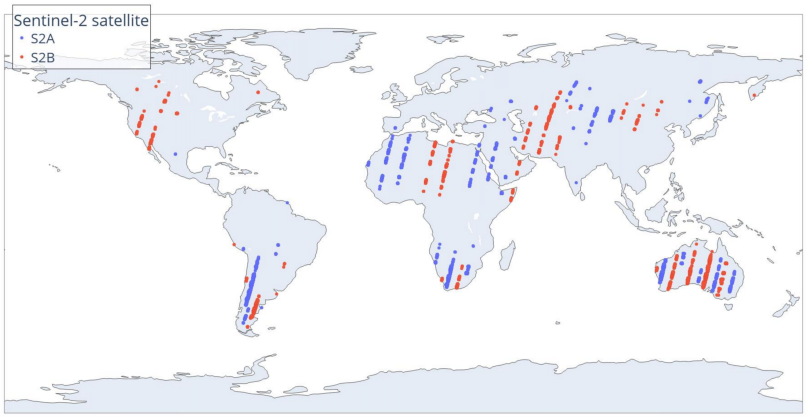

(a) Landsat-9 vs Sentinel-2 matchup locations

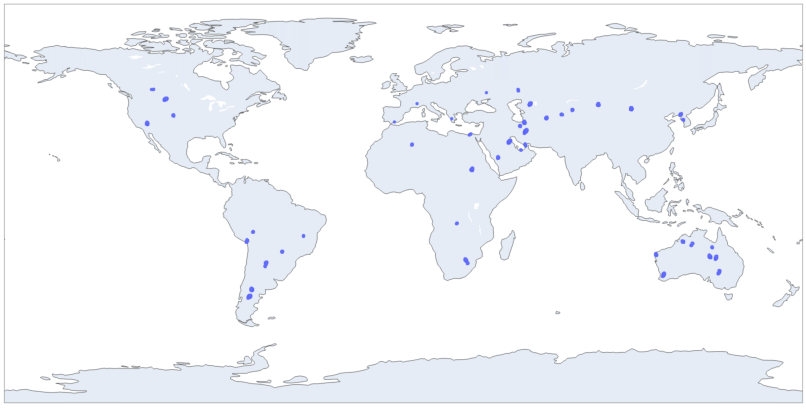

(b) Landsat-9 vs EMIT matchup locations

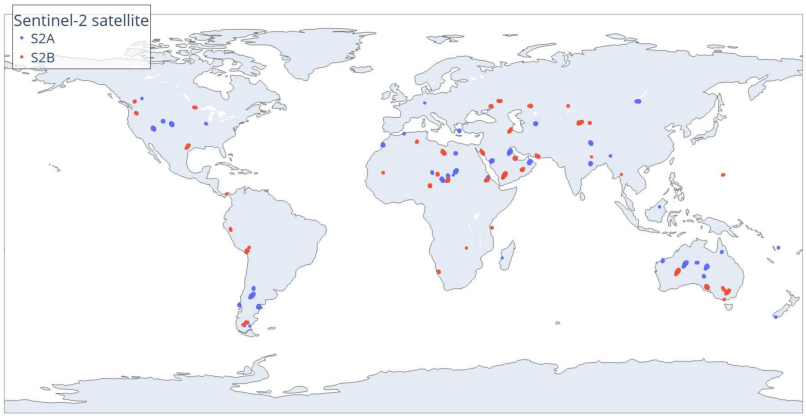

(c) Sentinel-2 vs EMIT matchup locations

Figure 2. Geographic distribution of the matchups used in the three cross-comparisons, for the NIR band: (a) L9 vs S2, (b) L9 vs EMIT, (c) S2 vs EMIT. The L9 vs S2 matchups follow the striped longitudinal pattern imposed by the overlap of the two Sun-synchronous repeat cycles, whereas the EMIT-based matchups are spread more uniformly across the globe within the latitude band sampled by the ISS orbit. In panels (a) and (c) blue and red dots distinguish matchups with S2A and S2B, respectively.

https://doi.org/10.5194/egusphere-2026-2803
Preprint. Discussion started: 18 June 2026

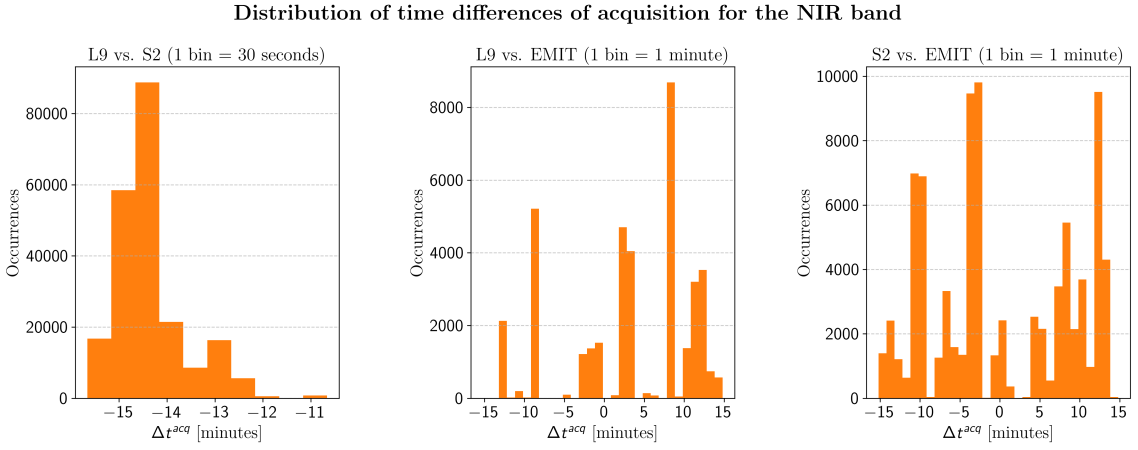

Figure 3. Histograms of the time difference of acquisition, Eq. (11), for the NIR band and the three cross-comparison cases: L9 vs S2 (left), L9 vs EMIT (centre), and S2 vs EMIT (right). The bin width is 30 s for the L9 vs S2 case and 1 min for the EMIT-based pairs. The L9 vs S2 distribution is concentrated around -14 min, reflecting the descending-node mean local solar time offset between the two Sun-synchronous orbits, while the L9 vs EMIT and S2 vs EMIT distributions are approximately symmetric around zero, as expected for matchups with the non-Sun-synchronous ISS orbit.

3.2.2 Angular distribution results

The angular sampling of the three matchup ensembles is now examined, starting from the viewing geometry of the individual missions and then moving to the per-matchup angular differences. Polar plots of the viewing zenith and viewing azimuth angles (VZA and VAA) for the NIR band are shown in Figure 4. The Landsat-9 viewing geometry forms a narrow, regular band around the centre of the polar plot at $\mathrm{VZA} \lesssim 5°$, consistent with the $\mathrm{VZA} < 5°$ filter applied in the L9 vs S2 ensemble (Section 2.3.6). Sentinel-2 covers a similar VZA range but with a broader and less coherent azimuthal sampling, plausibly reflecting the wider MSI swath (290 km against ~ 185 km for OLI-2; Drusch et al., 2012; Masek et al., 2020), which admits a larger range of cross-track positions over a given AOI under the same VZA cap, and the fact that the matchups draw from two satellites (S2A and S2B) sampling the same ground targets on different revisit days. EMIT samples the largest range of viewing zenith angles, with VZA typically between $5°$ and $10°$, consistent with the ISS pointing fluctuations reported by Roger et al. (2025). The L9 and EMIT VZA/VAA distributions are essentially band-independent, whereas the S2 distribution varies moderately between bands.

The per-matchup absolute angular differences—$|\Delta\mathrm{VZA}|$, $|\Delta\mathrm{VAA}|$ and $|\Delta\mathrm{SZA}|$—are reported as histograms in Figure 5 for the NIR band, separately for the L9 vs S2 pair (panel a) and the two EMIT-based pairs (panel b, with the two cases overlaid). The two panels are presented separately because the L9 vs S2 ensemble is approximately one order of magnitude larger than the two EMIT-based ensembles (Table 5) and the latter are of comparable cardinality, so that the overlaid representation in panel (b) is informative whereas pooling the three cases on a common axis is not.

https://doi.org/10.5194/egusphere-2026-2803
Preprint. Discussion started: 18 June 2026

Band	Cross-comparison case	Minimum	Maximum	Mean	Std deviation
Blue	L9 vs S2	-15 min 46 s	-10 min 21 s	-14 min 26 s	0 min 42 s
	L9 vs EMIT	-12 min 34 s	15 min 22 s	2 min 58 s	7 min 18 s
	S2 vs EMIT	-15 min 11 s	15 min 32 s	-0 min 4 s	8 min 49 s
Green	L9 vs S2	-15 min 46 s	-10 min 21 s	-14 min 27 s	0 min 40 s
	L9 vs EMIT	-12 min 34 s	14 min 18 s	3 min 16 s	7 min 23 s
	S2 vs EMIT	-15 min 11 s	15 min 32 s	-0 min 12 s	8 min 54 s
Red	L9 vs S2	-15 min 46 s	-10 min 21 s	-14 min 23 s	0 min 42 s
	L9 vs EMIT	-14 min 56 s	14 min 18 s	3 min 32 s	7 min 29 s
	S2 vs EMIT	-15 min 11 s	15 min 32 s	-0 min 24 s	8 min 55 s
NIR	L9 vs S2	-15 min 24 s	-10 min 21 s	-14 min 21 s	0 min 43 s
	L9 vs EMIT	-12 min 34 s	14 min 14 s	3 min 15 s	7 min 47 s
	S2 vs EMIT	-15 min 11 s	15 min 32 s	0 min 12 s	8 min 50 s
SWIR1	L9 vs S2	-15 min 42 s	-10 min 21 s	-14 min 19 s	0 min 44 s
	L9 vs EMIT	-12 min 34 s	14 min 14 s	3 min 41 s	7 min 47 s
	S2 vs EMIT	-15 min 11 s	15 min 32 s	-0 min 26 s	8 min 48 s
SWIR2	L9 vs S2	-15 min 42 s	-10 min 21 s	-14 min 19 s	0 min 44 s
	L9 vs EMIT	-14 min 56 s	15 min 24 s	3 min 47 s	7 min 40 s
	S2 vs EMIT	-15 min 11 s	15 min 32 s	-0 min 56 s	8 min 44 s

Table 6. Statistical characterization of the time difference of acquisition distributions, for the different bands and for each cross-comparison case

For the L9 vs S2 pair, $|\Delta\mathrm{VZA}|$ decreases approximately linearly from zero to the maximum admissible value of $5°$, with most matchups concentrated below $2°$. The shape is favourable for cross-comparison because matchups with nearly equal VZA are preferred when isolating radiometric differences. The $|\Delta\mathrm{VAA}|$ distribution, on the other hand, peaks around $180°$ in the visible bands, indicating that L9 and S2 view the matchup AOIs from opposite sides of nadir, as is typical of paired Sun-synchronous acquisitions; in the NIR, SWIR1, and SWIR2 bands the distribution broadens over the range $90°$–$210°$. The SZA difference distribution peaks around 2–$3°$, with S2 sampling systematically smaller SZA values than L9 by the same margin, consistent with the ~ 30-minute offset in mean local solar time at the descending node between the two missions (Section 3.2.1).

For the EMIT-based pairs, both the $|\Delta\mathrm{VZA}|$ and $|\Delta\mathrm{VAA}|$ distributions are essentially flat across their admissible ranges, with the only exception of the S2 vs EMIT $|\Delta\mathrm{VAA}|$, which exhibits a broad peak around $50°$ for all bands. Because EMIT does not orbit on a Sun-synchronous plane, no privileged viewing geometry is enforced relative to the multispectral missions: the matchups sample the angular space approximately uniformly within the filter limits. The $|\Delta\mathrm{SZA}|$ distributions remain narrow

https://doi.org/10.5194/egusphere-2026-2803
Preprint. Discussion started: 18 June 2026

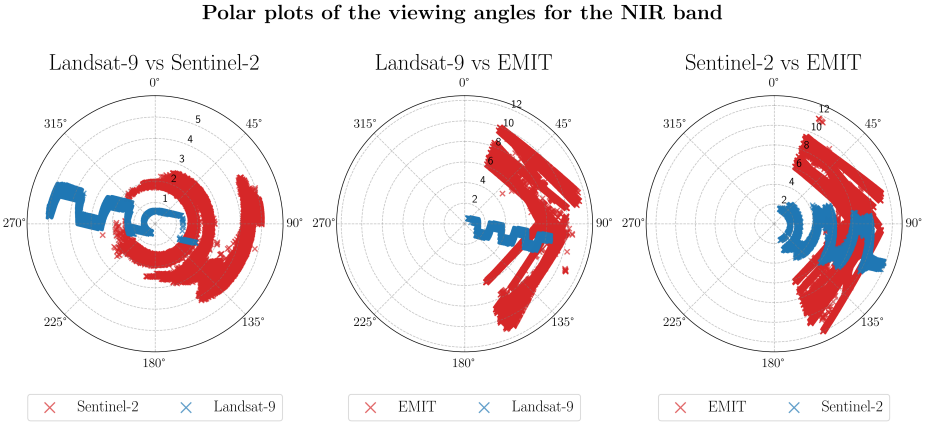

Figure 4. Polar plots of the viewing geometry (VZA radial, VAA azimuthal) for the NIR band: L9 vs S2 (left), L9 vs EMIT (centre), and S2 vs EMIT (right). Landsat-9 and Sentinel-2 acquire near-nadir, with VZA $< 5°$; EMIT samples a broader VZA range of approximately $5°$–$10°$ owing to the ISS pointing fluctuations.

for both EMIT-based pairs, since the solar geometry over a given target on a given day is essentially fixed; the small residual spread reflects the few-minute time offsets between EMIT and the multispectral missions.

Taken together, the distributions in Sections 3.2.1 and 3.2.2 confirm the qualitative expectation behind the choice of EMIT as a transfer reference: the L9 vs S2 SNO pair is affected by systematic temporal and azimuthal biases imposed by the joint Sun-synchronous geometry, whereas the L9 vs EMIT and S2 vs EMIT pairs sample the time and angular spaces approximately uniformly.

3.3 TOA reflectance cross-comparison results

We now turn to the radiometric comparison itself. The matchup-mean TOA reflectance values of the two missions in each pair, computed as described in Section 2.3.4, are summarised through a linear regression of the form of Eq. (1). In a cross-calibration context the two sensors play asymmetric roles, with one acting as the reference (independent variable) and the other being calibrated against it. In the present cross-comparison neither sensor is the reference and the assignment is a matter of convention. We adopt the following convention throughout:

- for the direct L9 vs S2 pair, OLI-2 acts as the independent variable, so that the regression has ρ_{L9}^{TOA} on the abscissa and ρ_{S2}^{TOA} on the ordinate;
- for the two EMIT-based pairs, EMIT acts as the independent variable, so that the regressions have ρ_{EMIT}^{TOA} on the abscissa and either ρ_{L9}^{TOA} or ρ_{S2}^{TOA} on the ordinate.

For a generic band B_x, the resulting linear relationships are

$$\rho_{S2}^{TOA,B_x} = a_{S2,L9}^{B_x} \rho_{L9}^{TOA,B_x} + b_{S2,L9}^{B_x}, \tag{12}$$

https://doi.org/10.5194/egusphere-2026-2803
Preprint. Discussion started: 18 June 2026

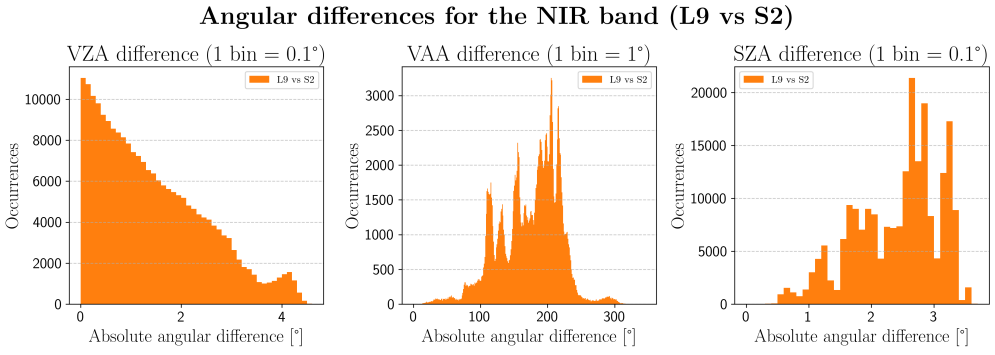

(a) L9 vs S2 cross-comparison

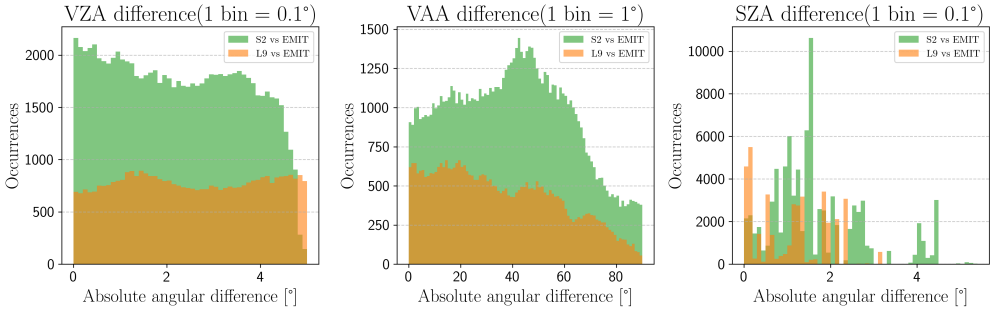

(b) Cross-comparisons with EMIT

Figure 5. Absolute angular differences (VZA, VAA, and SZA) for the NIR band: (a) L9 vs S2 and (b) the two EMIT-based pairs overlaid. The L9 vs S2 $|\Delta\mathrm{VAA}|$ distribution peaks around $180°$, indicating that the two missions view the target from opposite sides of nadir, and the $|\Delta\mathrm{VZA}|$ distribution decreases linearly from zero up to the $5°$ cut. The EMIT-based distributions of $|\Delta\mathrm{VZA}|$ are approximately flat, consistent with the broader VZA range sampled by EMIT, while the $|\Delta\mathrm{VAA}|$ distribution of the S2 vs EMIT pair peaks around $50°$ and that of the L9 vs EMIT pair is nearly uniform.

for the L9 vs S2 pair, and

$$\rho_{L9}^{TOA,B_x} = a_{L9,EMIT}^{B_x}\,\rho_{EMIT}^{TOA,B_x} + b_{L9,EMIT}^{B_x}, \tag{13}$$

$$\rho_{S2}^{TOA,B_x} = a_{S2,EMIT}^{B_x}\,\rho_{EMIT}^{TOA,B_x} + b_{S2,EMIT}^{B_x}, \tag{14}$$

for the L9 vs EMIT and S2 vs EMIT pairs, respectively. The L9 vs S2 regression is applied to the SBAF-corrected MSI reflectance defined in Section 2.3.7, whereas the EMIT-based regressions operate directly on the band-equivalent EMIT reflectance obtained from the hyperspectral convolution (Section 2.3.4) and therefore do not require any a-priori spectral correction. The S2 vs EMIT regression is further built on the EMIT reflectance rescaled to the Chance and Kurucz irradiance

https://doi.org/10.5194/egusphere-2026-2803
Preprint. Discussion started: 18 June 2026

convention, as detailed in Section 2.3.4, so that the L9–EMIT and S2–EMIT branches share a common irradiance reference and the EMIT contribution cancels exactly in the indirect L9 vs S2 comparison (Section 3.3.2).

3.3.1 TOA reflectance scatter plots

The matchup TOA reflectance ensembles for the three sensor pairs are shown as scatter plots in Figure 6. Each point corresponds to the AOI-mean TOA reflectance of one matchup, computed as described in Section 2.3.4. The scatter plots are shown for all six bands and for the S2A measurements; the equivalent plots for S2B are reported in the Appendix and lead to consistent conclusions. The independent variable on the abscissa follows the convention introduced in Section 3.3: ρ_{L9}^{TOA} for the L9 vs S2 panels and ρ_{EMIT}^{TOA} for the two EMIT-based panels.

The calibration curves overlaid on each panel (blue solid line for the red and the SWIR1 bands and red solid lines for the remaining bands) are obtained by fitting the matchups with a Huber regressor, which is preferred to ordinary least squares because it down-weights the residual outliers that survive the filtering step. The dashed black line is the 1:1 line, included for visual reference. The coefficient of determination r^2 is reported in each panel and exceeds 0.97 for all bands and all three pairs, indicating that a linear model captures the relationship between the two sensors to a very good approximation across the full reflectance range admitted by the filters. The dispersion of the matchups around the regression line grows mildly toward longer wavelengths, and the absolute number of outliers grows accordingly; this is consistent with the increasing matchup count from blue to SWIR2 (Table 5) and with the larger atmospheric variability typically encountered in the SWIR spectral region.

3.3.2 Calibration curves obtained

The slopes and intercepts of the regressions shown in Figure 6 are the *calibration curves* for the three sensor pairs. Those of the L9 vs EMIT, S2A vs EMIT and S2B vs EMIT comparisons are reported in Table 7. In the visible and NIR bands, the EMIT-based curves are very close to the 1:1 line: slopes lie between 0.967 and 1.007 and intercepts are below 0.006 in absolute value, which corresponds to sub-percent agreement at typical TOA reflectance values. The agreement is weaker in the SWIR bands, where the L9 vs EMIT slope drops to approximately 0.93 in SWIR1 and SWIR2, signalling a larger residual between L9 and EMIT in the shortwave infrared compared to the visible and NIR. The S2 vs EMIT slopes remain closer to unity (~ 0.95–0.97) in the same bands, so the discrepancy is asymmetric between the two EMIT branches.

Combining the L9 vs EMIT and the S2 vs EMIT calibration curves through the double-differencing scheme of Eq. (2) yields the *indirect* L9 vs S2 calibration curve. Equating Eqs. (13) and (14) through ρ_{EMIT}^{TOA,B_x} gives, for the generic band B_x,

$$\rho_{S2}^{TOA,B_x} = a_{S2,L9(EMIT)}^{B_x}\,\rho_{L9}^{TOA,B_x} + b_{S2,L9(EMIT)}^{B_x}\,, \tag{15}$$

https://doi.org/10.5194/egusphere-2026-2803
Preprint. Discussion started: 18 June 2026

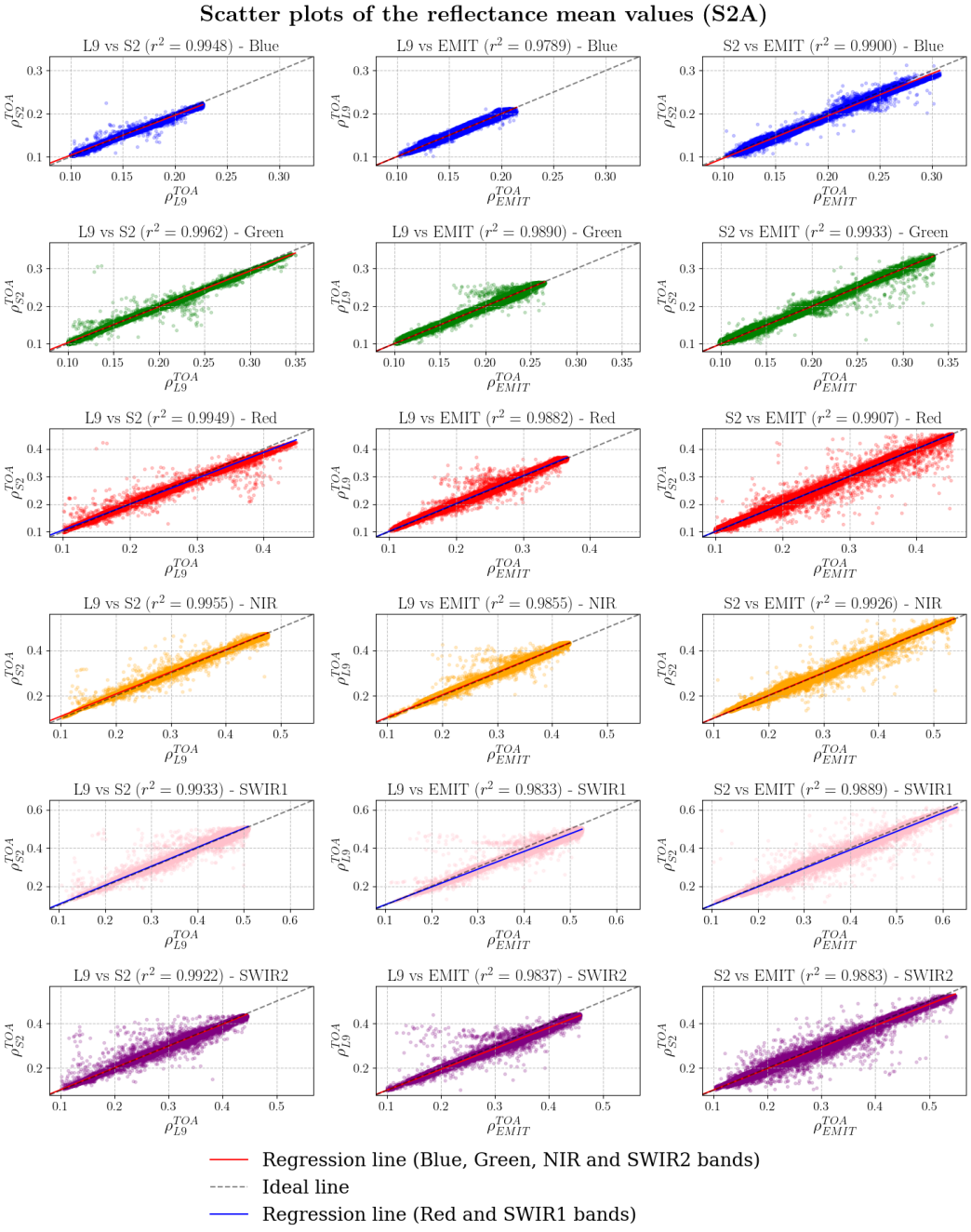

Figure 6. Matchup TOA reflectance scatter plots for the three cross-comparison cases (L9 vs S2, L9 vs EMIT, S2 vs EMIT) and the six spectral bands, for the S2A measurements. The blue solid line is the Huber regression and the black dashed line is the 1:1 reference. The independent variable on the abscissa follows the convention of Section 3.3. The coefficient of determination r^2 exceeds 0.97 in all panels.

https://doi.org/10.5194/egusphere-2026-2803
Preprint. Discussion started: 18 June 2026

Band	L9 vs EMIT	S2A vs EMIT	S2B vs EMIT
Blue	$\mathrm{L9} = 0.9951\ \mathrm{EMIT} + 0.0008$	$\mathrm{S2} = 0.9828\ \mathrm{EMIT} - 0.0019$	$\mathrm{S2} = 0.9671\ \mathrm{EMIT} + 0.0020$
Green	$\mathrm{L9} = 0.9964\ \mathrm{EMIT} + 0.0005$	$\mathrm{S2} = 1.0003\ \mathrm{EMIT} - 0.0008$	$\mathrm{S2} = 0.9989\ \mathrm{EMIT} + 0.0011$
Red	$\mathrm{L9} = 1.0045\ \mathrm{EMIT} + 0.0011$	$\mathrm{S2} = 0.9964\ \mathrm{EMIT} + 0.0014$	$\mathrm{S2} = 0.9984\ \mathrm{EMIT} + 0.0010$
NIR	$\mathrm{L9} = 0.9909\ \mathrm{EMIT} + 0.0055$	$\mathrm{S2} = 1.0023\ \mathrm{EMIT} + 0.0010$	$\mathrm{S2} = 1.0073\ \mathrm{EMIT} - 0.0009$
SWIR1	$\mathrm{L9} = 0.9289\ \mathrm{EMIT} + 0.0096$	$\mathrm{S2} = 0.9655\ \mathrm{EMIT} + 0.0030$	$\mathrm{S2} = 0.9690\ \mathrm{EMIT} + 0.0010$
SWIR2	$\mathrm{L9} = 0.9355\ \mathrm{EMIT} + 0.0075$	$\mathrm{S2} = 0.9614\ \mathrm{EMIT} + 0.0054$	$\mathrm{S2} = 0.9545\ \mathrm{EMIT} + 0.0046$

Table 7. Calibration curve equations for the EMIT cross-comparisons, obtained fitting the mean TOA reflectance values in the scatter plots with the Huber regressor, which is less sensible to the outliers.

where the subscript $(EMIT)$ denotes that the indirect slope and intercept are obtained from the two EMIT-based regressions. The two coefficients are given by

$$a^{B_x}_{S2,L9(EMIT)} = \frac{a^{B_x}_{S2,EMIT}}{a^{B_x}_{L9,EMIT}}, \tag{16a}$$

$$b^{B_x}_{S2,L9(EMIT)} = b^{B_x}_{S2,EMIT} - \left(\frac{a^{B_x}_{S2,EMIT}}{a^{B_x}_{L9,EMIT}}\right) b^{B_x}_{L9,EMIT}\,. \tag{16b}$$

By construction, this indirect comparison no longer requires an a-priori SBAF between OLI-2 and MSI (the spectral matching is absorbed in the convolution of the EMIT spectrum onto the corresponding multispectral band), and the contribution of the EMIT absolute calibration cancels exactly to first order in Eq. (16a)–(16b).

Table 8 compares the direct and the indirect L9 vs S2 calibration curves, separately for S2A and S2B. Two observations stand out. First, in the visible and NIR bands, the indirect slopes are systematically closer to unity and the indirect intercepts are systematically smaller in absolute value than the direct ones. For example, the indirect blue-band slope for the L9 vs S2A pair is 0.988, against 0.926 in the direct case, with the indirect intercept reduced from 0.011 to -0.003; similar reductions are observed for green, red, and NIR. This is the expected behaviour if the residual radiometric offset between OLI-2 and MSI is small: removing the SBAF and the geometric biases through the EMIT branch brings the two missions into closer alignment. Second, the SWIR1 and SWIR2 bands show the opposite trend: the indirect slopes (~ 1.04) move further from unity than the direct ones (~ 0.98–1.00). This is consistent with the asymmetry already noted in Table 7, where the L9 vs EMIT branch has a slope of ~ 0.93 in the SWIR bands: the double-differencing scheme propagates this residual into the indirect L9 vs S2 comparison through Eq. (16a), magnifying rather than reducing the apparent mismatch in this spectral region. The quantitative implications of this behaviour for the radiometric agreement between L9 and S2 are examined in Section 3.4.

https://doi.org/10.5194/egusphere-2026-2803
Preprint. Discussion started: 18 June 2026

Band	L9 vs S2A		L9 vs S2B	
	Direct	Using EMIT	Direct	Using EMIT
Blue	$S2 = 0.9263\,L9 + 0.0109$ $(L9 = 1.0797\,S2 - 0.0118)$	$S2 = 0.9876\,L9 - 0.0027$ $(L9 = 1.0126\,S2 + 0.0027)$	$S2 = 0.9609\,L9 + 0.0067$ $(L9 = 1.0407\,S2 - 0.0070)$	$S2 = 0.9719\,L9 + 0.0012$ $(L9 = 1.029\,S2 - 0.0012)$
Green	$S2 = 0.9535\,L9 + 0.0076$ $(L9 = 1.0487\,S2 - 0.0080)$	$S2 = 1.0039\,L9 - 0.0013$ $(L9 = 0.9961\,S2 + 0.0013)$	$S2 = 0.9695\,L9 + 0.0060$ $(L9 = 1.0315\,S2 - 0.0062)$	$S2 = 1.0025\,L9 + 0.0006$ $(L9 = 0.9975\,S2 - 0.0006)$
Red	$S2 = 0.9366\,L9 + 0.0122$ $(L9 = 1.0677\,S2 - 0.0130)$	$S2 = 0.9919\,L9 + 0.0003$ $(L9 = 1.0082\,S2 - 0.0003)$	$S2 = 0.9324\,L9 + 0.0147$ $(L9 = 1.0726\,S2 - 0.0158)$	$S2 = 0.9939\,L9 - 0.0001$ $(L9 = 1.0061\,S2 + 0.0001)$
NIR	$S2 = 0.9767\,L9 + 0.0120$ $(L9 = 1.0239\,S2 - 0.0123)$	$S2 = 1.0115\,L9 - 0.0046$ $(L9 = 0.9886\,S2 + 0.0045)$	$S2 = 0.9787\,L9 + 0.0123$ $(L9 = 1.0218\,S2 - 0.0126)$	$S2 = 1.0166\,L9 - 0.0065$ $(L9 = 0.9834\,S2 + 0.0064)$
SWIR1	$S2 = 0.9955\,L9 + 0.0052$ $(L9 = 1.0045\,S2 - 0.0052)$	$S2 = 1.0405\,L9 - 0.0070$ $(L9 = 0.9612\,S2 + 0.0067)$	$S2 = 0.9823\,L9 + 0.0077$ $(L9 = 1.0180\,S2 - 0.0078)$	$S2 = 1.0432\,L9 - 0.0090$ $(L9 = 0.9586\,S2 + 0.0086)$
SWIR2	$S2 = 0.9795\,L9 + 0.0052$ $(L9 = 1.0209\,S2 - 0.0053)$	$S2 = 1.0277\,L9 - 0.0023$ $(L9 = 0.9730\,S2 + 0.0022)$	$S2 = 0.9831\,L9 + 0.0072$ $(L9 = 1.0172\,S2 - 0.0073)$	$S2 = 1.0203\,L9 - 0.0031$ $(L9 = 0.9801\,S2 + 0.0030)$

Table 8. Calibration curve equations for the *direct* and *indirect* L9 vs S2 cross-comparisons. For the *direct* one, they are obtained fitting the mean TOA reflectance values in the scatter plots using the Huber regressor, which is less sensible to the outliers. Fot the *indirect* cross-comparison, equations were found using the double differencing method, where the *slope* and *intercept* are found using (16b) and (16b) respectively. In the cross-comparisons where EMIT is used as a calibration transfer, *bias* values result to be smaller and *slope* values are closer to one, for all bands except for the SWIR1 and SWIR2 bands.

3.4 TOA reflectance relative error assessment

In this last section, the reflectance relative error is calculated from the calibration curves obtained, preferred to the absolute errors because it is directly comparable with the measurements uncertainties. Firstly, it is done for the three cross-comparison couples separately and, finally, also for the indirect Landsat-9 vs Sentinel-2 cross-comparison.

3.4.1 Error definition

Although the slopes and intercepts of the calibration curves provide a compact summary of the comparison, the radiometric agreement between the two sensors is more naturally expressed as a relative error in TOA reflectance, which can be directly contrasted with the radiometric measurement uncertainties of the individual instruments (Section 2.1).

The relative error of S_2 with respect to S_1 is defined as

$$\epsilon_{S_2}\left(\rho_{S_1}^{TOA}\right) = \frac{\rho_{S_2}^{TOA}\left(\rho_{S_1}^{TOA}\right) - \rho_{S_1}^{TOA}}{\rho_{S_1}^{TOA}}, \tag{17}$$

https://doi.org/10.5194/egusphere-2026-2803
Preprint. Discussion started: 18 June 2026

where $\rho_{S_2}^{TOA}(\rho_{S_1}^{TOA})$ is the value of the dependent-sensor reflectance predicted by the corresponding calibration curve at a given value of the independent-sensor reflectance $\rho_{S_1}^{TOA}$. Substituting the linear regression $\rho_{S_2}^{TOA} = a\,\rho_{S_1}^{TOA} + b$ into Eq. (17) gives the identity

$$\epsilon_{S_2}\left(\rho_{S_1}^{TOA}\right) \;=\; (a-1) + \frac{b}{\rho_{S_1}^{TOA}}\,, \tag{18}$$

so that the relative error is a horizontal asymptote at $(a-1)$ to which the $b/\rho_{S_1}^{TOA}$ term adds a $1/\rho$ correction whose amplitude is set by the magnitude and sign of the regression intercept. When b is small relative to $|a-1|\,\rho_{S_1}^{TOA}$, the error curve is approximately flat at $(a-1)$ across the plotted reflectance range; when b is comparable to or larger than that product, the curve bends away from $(a-1)$ toward smaller reflectance values, with the sign of b controlling whether the curve rises or falls.

The quantity defined by Eq. (17) is computed for the three direct cross-comparisons in Section 3.4.2 and for the indirect L9 vs S2 comparison in Section 3.4.3, using in each case the slope and intercept of the corresponding calibration curve. We restrict the plots to the reflectance range used to build the regressions, that is, from $\rho^{TOA} = 0.1$ to the per-band 95th percentile of the distribution (Section 2.3.6).

3.4.2 Direct cross-comparison results

The relative-error curves obtained from the three direct cross-comparisons are shown in Figure 7a for the matchups built with S2A and in Figure 7b for those built with S2B. Each figure displays the six bands jointly in three side-by-side panels: L9 vs S2 (left), L9 vs EMIT (centre), and S2 vs EMIT (right). The two figures share the L9 vs EMIT panel, which is independent of the S2 platform.

On the horizontal axis of each panel is the AOI-mean TOA reflectance of the independent sensor (Section 3.3), spanning the reflectance range $[0.1, P_{95}]$ used to build the regressions (Section 2.3.6). On the vertical axis is the relative percentage error of the dependent sensor with respect to the independent one, Eq. (17). The black dashed lines mark the combined radiometric uncertainty of the corresponding sensor pair, taken as the root sum squared (RSS) of the individual instrument uncertainties given in Section 2.1 ($3\,\%$ for L9 and S2, $5\,\%$ for EMIT):

- $\mathrm{RSS}_{L9,S2} = \sqrt{3^2+3^2} \simeq 4.23\,\%$ for the L9 vs S2 comparison;
- $\mathrm{RSS}_{L9,EMIT} = \mathrm{RSS}_{S2,EMIT} = \sqrt{3^2+5^2} \simeq 5.83\,\%$ for the two EMIT-based comparisons.

In all three direct comparisons, the relative error lies within the combined uncertainty band for reflectance values above approximately 0.2, across all six spectral bands and for both Sentinel-2 platforms. Below this threshold the curves diverge as expected from Eq. (17), with the divergence driven by the intercept term b/ρ^{TOA}. The compatibility of all three direct comparisons with the combined measurement uncertainty over the bulk of the reflectance range supports the validity of the global-scale matchup methodology proposed here and provides the radiometric baseline against which the indirect L9 vs S2 comparison is assessed in the following section.

https://doi.org/10.5194/egusphere-2026-2803
Preprint. Discussion started: 18 June 2026

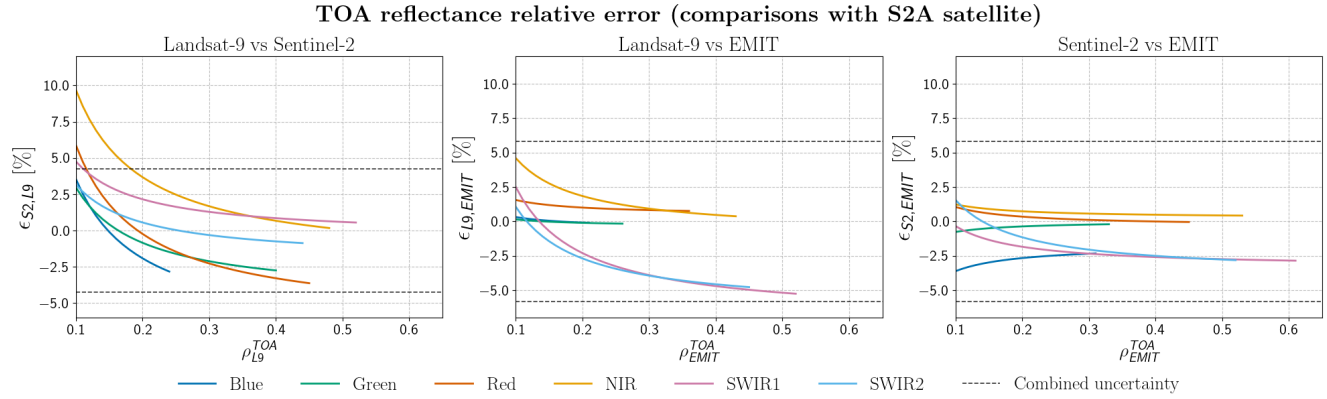

(a) Sentinel-2A measurements

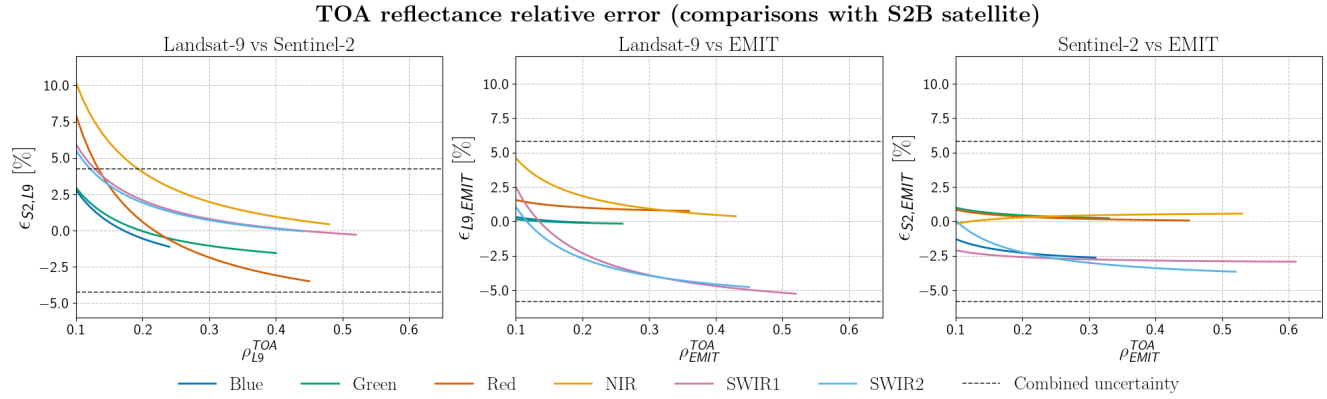

(b) Sentinel-2B measurements

Figure 7. Relative percentage error of TOA reflectance, Eq. (17), for the three direct cross-comparisons and for the six spectral bands: (a) L9 vs S2A and the corresponding L9 vs EMIT and S2A vs EMIT panels, and (b) the same with S2B in place of S2A. The black dashed lines mark the combined uncertainty of each pair (4.23 % for L9 vs S2, 5.83 % for the EMIT-based pairs). The L9 vs EMIT panels in (a) and (b) are identical, since the comparison does not involve Sentinel-2.

3.4.3 Indirect cross-comparison results

The relative-error analysis is now extended to the indirect L9 vs S2 comparison obtained through the double-differencing scheme of Section 3.3.2. Before discussing the results, it is worth recalling the structural differences between the direct and the indirect L9 vs S2 comparisons, since these motivate the contrasts presented below. The direct comparison is affected by (i) the
505 residual spectral mismatch between the OLI-2 and MSI bands, which is corrected through an a-priori SBAF (Section 2.3.7), and (ii) the systematic temporal and azimuthal biases imposed by the two Sun-synchronous orbits, documented in Sections 3.2.1 and 3.2.2. The indirect comparison, by construction, removes both: the spectral matching is absorbed in the convolution of the EMIT spectrum onto the multispectral SRFs, and the EMIT-based matchups sample a much more symmetric set of viewing and

https://doi.org/10.5194/egusphere-2026-2803
Preprint. Discussion started: 18 June 2026

illumination geometries. Provided that any residual sensitivity to the EMIT absolute calibration cancels in the double difference (a condition discussed in Section 2.3.4 and revisited in the discussion below), the residual L9 vs S2 differences in the indirect comparison can be attributed to genuine radiometric offsets between OLI-2 and MSI, modulated by atmospheric effects that affect the two missions differently because of their slightly different illumination geometries.

The relative errors of the indirect L9 vs S2 comparison are computed by inserting the indirect slopes and intercepts of Eqs. (16a) and (16b) into Eq. (17). For readability, the resulting error curves are split into two figures, one for the visible bands (Figure 8) and one for the NIR and SWIR bands (Figure 9). Each figure has four panels: the left column shows the direct L9 vs S2 error curves (already displayed in Figure 7, reproduced here for ease of comparison) and the right column shows the corresponding indirect L9 vs S2 curves; the top row uses S2A and the bottom row S2B. The solid part of each curve covers the reflectance range used to build the regression ($[0.1, P_{95}]$) and the dashed extension is shown only for visual reference beyond this range. The dashed black lines at $\pm 4.23\,\%$ mark the combined $3\,\%$-by-$3\,\%$ uncertainty of the L9 vs S2 comparison.

Figure 8 shows the results for the blue, green and red bands. In the indirect comparison, the relative error is essentially *constant* as a function of reflectance, between approximately $-2.5\,\%$ and zero across the full reflectance range and the two S2 platforms. This is the expected signature of a calibration curve with slope close to unity and a small intercept (Table 8): the indirect slopes deviate from one by less than $1.5\,\%$ in the visible bands and the indirect intercepts are smaller than the direct ones by roughly an order of magnitude, suppressing the low-reflectance divergence that characterises the direct comparison. The indirect errors are consistent across the three visible bands and the two platforms, with the largest residual offset ($-2.5\,\%$) systematically observed in the blue band and sub-percent agreement in the green and red bands. By contrast, the direct L9 vs S2 error curves vary substantially with both band and platform: the S2A curves show similar behaviour across the three visible bands (decreasing from about $+5\,\%$ at $\rho^{TOA} \sim 0.1$ to a few percent below zero at the high-reflectance end), whereas the S2B curves show a markedly larger red-band error, which is most plausibly attributed to the SBAF coefficients used in the direct comparison, derived for the OLI/MSI-A pair and applied here also to MSI-B (Section 2.3.7).

Figure 9 shows the NIR, SWIR1, and SWIR2 bands. The behaviour of the three bands is now sufficiently band-specific to be discussed separately.

NIR band. In both the direct and the indirect comparison, the NIR error approaches zero at large reflectance, but the convergence is reached at smaller reflectances in the indirect case. In the direct comparison, the curve starts at approximately $+10\,\%$ at $\rho^{TOA} = 0.1$, crosses the combined uncertainty band only above $\rho^{TOA} \simeq 0.2$, and approaches zero only at the high-reflectance end of the range. In the indirect comparison the curve starts at approximately $-5\,\%$ and asymptotes to within $\pm 0.5\,\%$ already for $\rho^{TOA} \gtrsim 0.3$, that is, over the range that primarily samples bare or sparsely vegetated soil surfaces in this part of the spectrum—the surface types admitted by the $[0, 0.2]$ NDVI filter and considered most suitable for cross-calibration. The Landsat-9 band 5 and Sentinel-2 band 8A used here are both centred near 865 nm, a spectral window largely insensitive to water-vapour absorption (Tan et al., 2020) and weakly affected by Rayleigh scattering, so the close-to-zero agreement found in the indirect comparison is consistent with the expectation that the NIR offset of the direct comparison is dominated by the SBAF and geometric biases rather than by a residual radiometric mismatch between OLI-2 and MSI.

https://doi.org/10.5194/egusphere-2026-2803
Preprint. Discussion started: 18 June 2026

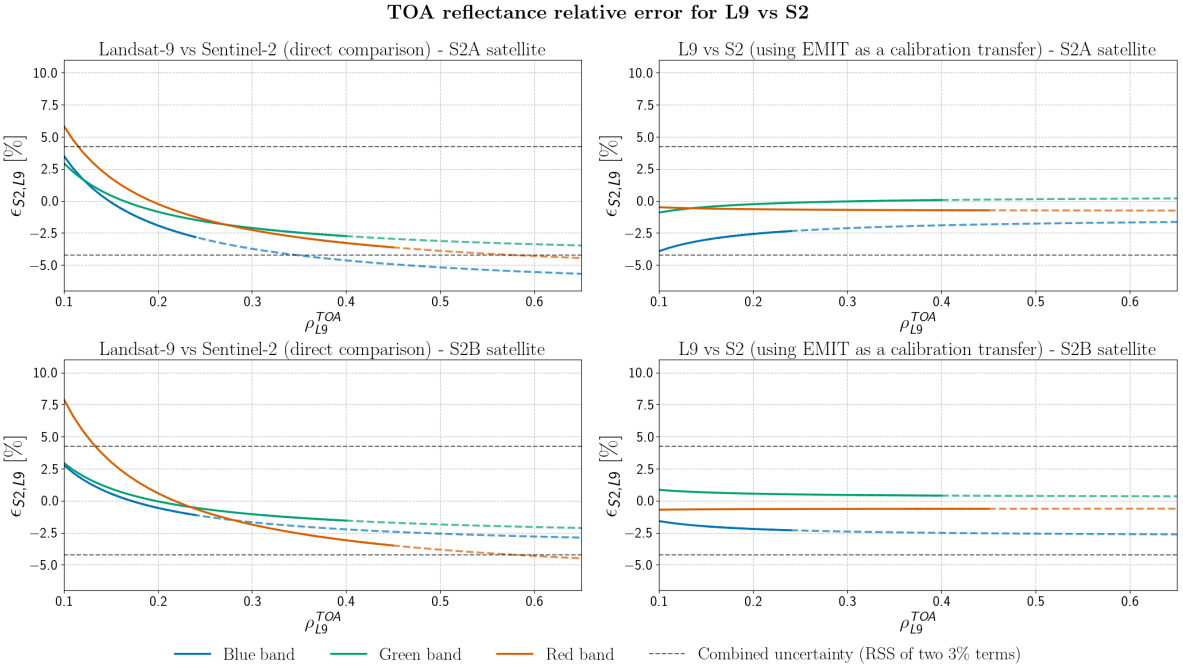

Figure 8. Relative percentage error of TOA reflectance for the direct (left) and indirect (right) L9 vs S2 comparisons in the visible bands. Top row: S2A; bottom row: S2B. The solid part of each curve covers the reflectance range used to build the regression and the dashed extension is shown only for reference. The dashed black lines mark the combined uncertainty of $\pm 4.23\,\%$. In the indirect comparison the relative error is nearly constant and lies between $-2.5\,\%$ and zero, with the largest residual in the blue band, whereas the direct comparison shows a wider band-dependent range and a marked platform asymmetry, most visible in the red band of S2B.

SWIR1 and SWIR2 bands. The direct SWIR errors are well-behaved and follow the same general pattern as the NIR, with values below the combined uncertainty across most of the reflectance range. The indirect SWIR errors, by contrast, exhibit a positive bias that grows with reflectance and reaches up to $+2.5\,\%$ at the high-reflectance end of the range. This is the radiometric counterpart of the slope behaviour already noted in Table 8: the indirect L9 vs S2 SWIR slopes are approximately 1.04, against ~ 0.98–1.00 in the direct case. From Eq. (16a), the indirect slope is the ratio of the S2 vs EMIT slope to the L9 vs EMIT slope, and Table 7 shows that the latter drops to ~ 0.93 in the SWIR bands while the former remains close to ~ 0.96. The SWIR offset of the indirect L9 vs S2 comparison is therefore driven mostly by the L9 vs EMIT branch of the double difference and, accordingly, its magnitude tracks the larger uncertainty of this branch in the SWIR region (centre panel of Figure 7, where the L9 vs EMIT SWIR curves are the only ones to approach the $\pm 5.83\,\%$ combined-uncertainty envelope of that pair). The implications of this residual—and possible explanations in terms of EMIT radiometric performance in the SWIR, residual spectral-convolution asymmetries, or atmospheric directionality—are revisited in the discussion.

Considered together, the indirect L9 vs S2 results display a behaviour that contrasts qualitatively with that of the direct comparison: the relative error is largely independent of reflectance and band-specific in sign and magnitude. This is the expected

https://doi.org/10.5194/egusphere-2026-2803
Preprint. Discussion started: 18 June 2026

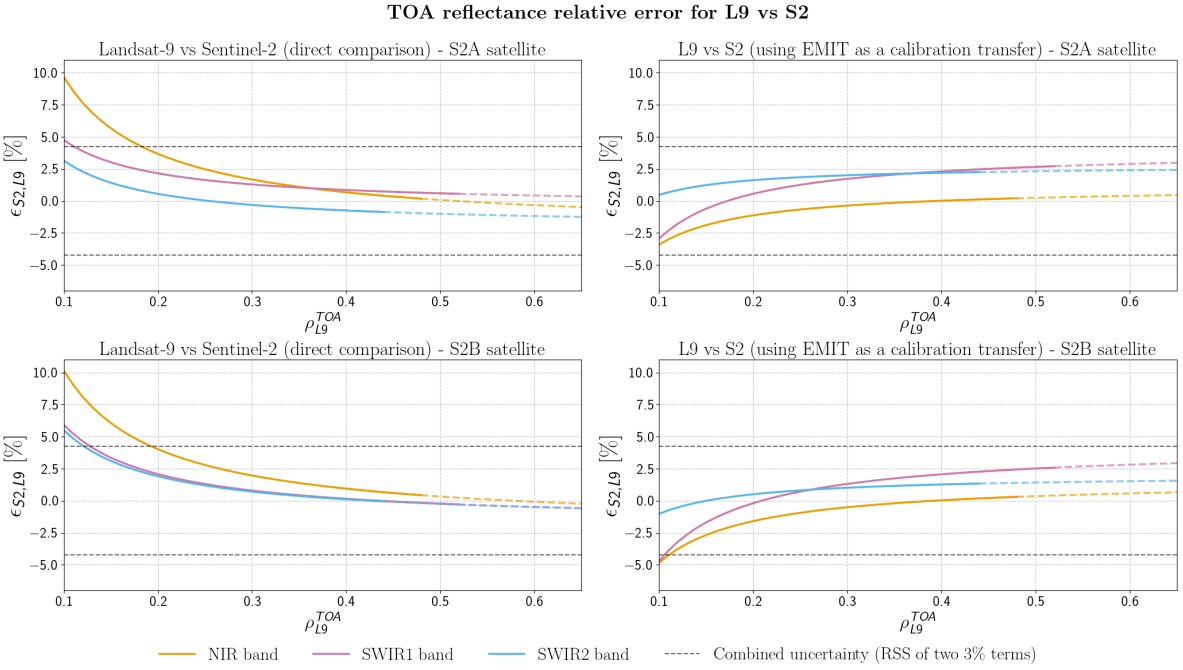

Figure 9. Relative percentage error of TOA reflectance for the direct (left) and indirect (right) L9 vs S2 comparisons in the NIR, SWIR1, and SWIR2 bands. Top row: S2A; bottom row: S2B. The solid part of each curve covers the reflectance range used to build the regression and the dashed extension is shown only for reference. The dashed black lines mark the combined uncertainty of $\pm 4.23\,\%$. In the NIR band, the indirect comparison reaches sub-percent agreement already at $\rho^{TOA} \gtrsim 0.3$, against $\gtrsim 0.5$ in the direct comparison. In the SWIR1 and SWIR2 bands the indirect comparison shows a positive bias of up to $+2.5\,\%$, inherited from the L9 vs EMIT branch of the double difference, where the calibration slope departs from unity more than in the other bands and pairs.

signature of a regression dominated by a near-unity slope and a small intercept, and it is consistent with the interpretation that the residual L9 vs S2 differences reflect genuine, percent-level radiometric offsets between OLI-2 and MSI, modulated by the residual directionality encoded in the matchup geometry. The implications of these findings for the L9–S2 interoperability and the limitations of the present analysis are discussed in the following section.

4 Discussion and conclusions

The indirect L9–S2 cross-comparison obtained through EMIT yields nearly constant biases in the visible bands, with agreement better than 1% in the green and red bands, approximately -2.5% in the blue band, and a positive bias of up to 2.5% in the shortwave-infrared bands. The near-infrared band agrees within 0.5% above a reflectance of 0.3. Once the contribution of the reference is removed through double differencing, the residual L9–S2 differences depend on band but are largely independent of reflectance, which is consistent with their interpretation as genuine radiometric offsets between OLI-2 and MSI rather than

https://doi.org/10.5194/egusphere-2026-2803
Preprint. Discussion started: 18 June 2026

as scene- or geometry-driven artefacts. Cross-calibration studies between OLI and MSI based on different methodologies have similarly reported band-dependent offsets at the percent level (Farhad et al., 2020; Pinto et al., 2016), supporting this interpretation. The SWIR offset is also consistent with the larger uncertainties of the L9–EMIT comparison in this spectral region (see Figure 7). Two contributions worth investigating in future work could nevertheless refine these values: residual asymmetries in the EMIT-to-OLI-2 and EMIT-to-MSI spectral convolutions if the underlying spectra in the L9–EMIT and S2–EMIT matchup ensembles do not have identical statistical distributions, and residual differences in surface and atmospheric directionality between the two missions, which would propagate independently into each branch. The non-linear behaviour of the relative error at low reflectance, more pronounced in the NIR and SWIR than in the visible, is harder to attribute unambiguously: it could reflect the larger dynamic range of these bands (including a non-linear response of the detector itself), residual offsets introduced by the linear regression at the lowest reflectance values, or a combination of the two. The fact that the non-linear part of the curve is consistent between S2A and S2B but the visible curves differ slightly between the two satellites suggests that the effect is not driven by a single dominant cause.

A natural concern with the proposed methodology is that, although it removes the need for an a-priori Spectral Band Adjustment Factor (SBAF) between L9 and S2, it still relies on a hyperspectral convolution of the EMIT spectrum onto the OLI-2 and MSI Spectral Response Functions. The residual effect of the spectral convolution is generally small relative to the bias values reported here (Gorroño et al., 2017; Stedman et al., 2025). In addition, because EMIT enters the L9–EMIT and S2–EMIT comparisons in the same way, any residual convolution effect tends to be correlated between the two pairs and therefore largely cancels in the double difference. The net advantages over a direct L9–S2 SNO comparison are thus that no a-priori SBAF coefficient must be assumed, that the angular and temporal mismatches are more symmetric thanks to the non-Sun-synchronous orbit of the reference, and that the comparison samples a wide range of surface and atmospheric conditions globally rather than the small number of bright, spectrally flat targets used by PICS-based methods.

A second methodological subtlety concerns the role of the solar irradiance model in the conversion from EMIT at-sensor radiance to TOA reflectance. In the Level-1 processing of Landsat-9 and Sentinel-2 the irradiance model is used both at the radiometric calibration of radiance and at the radiance-to-reflectance conversion, and its contribution cancels at the reflectance level: the L9 and S2 TOA reflectances entering this work are therefore insensitive to the choice of irradiance model. In contrast, the EMIT reflectance is computed via Eq. (4), in which the irradiance model was entered only once. As detailed in Section 2.3.4, the factor k in Eq. (4) is inferred from the multispectral mission through Eq. (5): its purpose is operational, namely to align EMIT with the multispectral mission in terms of band convolution, Sun-Earth distance and illumination geometry, not to suppress an irradiance-model error. As a consequence, the EMIT reflectance in each direct comparison inherits the irradiance model of the corresponding multispectral mission — Chance and Kurucz in the L9–EMIT branch and Thuillier in the S2–EMIT branch (Levy et al., 2024) — and each of the two direct comparisons carries a residual sensitivity to the irradiance model on the EMIT side. In the indirect L9–S2 comparison this residual cancels in the double difference, once the two branches are aligned onto a common irradiance convention as described in Section 2.3.4. The choice of common reference is arbitrary in this regard: any common convention — or none at all — would yield the same indirect result. Because the primary goal of this work is the indirect L9–S2 comparison, the irradiance-model residual that affects the two direct branches is a secondary issue and does not

https://doi.org/10.5194/egusphere-2026-2803
Preprint. Discussion started: 18 June 2026

propagate to the main deliverable. EMIT acts in the double-differencing scheme as a spectral and geometric anchor rather than as an absolute radiometric reference.

The most important limitation specific to EMIT is its mounting on the International Space Station. The ISS orbit, while non-Sun-synchronous and therefore beneficial for sampling a wide range of solar geometries, restricts EMIT's coverage to latitudes within roughly $\pm 52°$ and limits the number of EMIT acquisitions over the SNO targets considered here. Furthermore, EMIT pointing depends on the ISS orbit fluctuations and results in VZA values typically between $5°$ and $10°$ as shown in Figure 4 and consistent with the values reported in Roger et al. (2025). Thus, there is room for matchup optimisation and one that future work could address by combining other hyperspectral references in a single double-differencing framework. For example, CLARREO Pathfinder (Roithmayr et al., 2014) is designed to follow a nadir path and includes pointing capabilities while mounted on the ISS. A complementary direction would be to revisit the trade-off between the matchup filtering setup and the resulting ensemble size: relaxing or tightening the spatial, temporal, angular and spectral homogeneity criteria changes the number of available matchups, and a larger or differently selected ensemble would enable clustering the comparison by surface type (e.g. vegetation, bare soil, snow, water) so that the L9–S2 biases can be characterised separately for each regime rather than only at the global, scene-aggregated level reported here.

Site-based references such as Pseudo-Invariant Calibration Sites (Helder et al., 2013; Mishra et al., 2014) or the Radiometric Calibration Network (Bouvet et al., 2019) provide a natural alternative for the same kind of indirect cross-comparison, with the additional advantage of an SI-traceable surface anchor in the RadCalNet case. However, they are subject to limitations of their own. First, they constrain the comparison to a small number of fixed targets, which are typically bright, spectrally flat desert or salt-flat surfaces and therefore do not represent the full diversity of TOA spectra observed by L9 and S2 in operational use. Second, even 'stable' targets can be affected by long-term natural and anthropogenic change – dune migration, episodic precipitation, vegetation growth, or infrastructure development – whose contribution must be modelled or filtered and which sets a floor on the achievable comparison accuracy (Helder et al., 2013; Mishra et al., 2014). Third, because both L9 and S2 follow Sun-synchronous orbits, their overpasses over any given fixed site sample only a narrow band of solar and viewing geometries, so the resulting matchups remain affected by the directional issues that the SNO geometry is designed to suppress and require a BRDF model to be interpreted in absolute terms (Jing et al., 2019). The hyperspectral transfer-reference approach proposed here side-steps these difficulties by operating globally and over a wide range of surface types and atmospheric conditions, and by exploiting the non-Sun-synchronous orbit of EMIT to obtain a more symmetric angular sampling. The cost is that the comparison relies on the radiometric stability of the hyperspectral reference rather than on the absolute SI traceability of a ground-based site.

This study deliberately restricts the Landsat side of the comparison to Landsat-9 and does not include Landsat-8. Although the two platforms are near-identical, they carry distinct instruments (OLI on Landsat-8 and its successor OLI-2 on Landsat-9) that, while of similar design, cannot be treated as a single sensor. In contrast, Sentinel-2 units carry a common MSI design. Adding Landsat-8 would therefore introduce a further instrument and an additional set of direct EMIT comparisons, increasing the data processing and the complexity of the exposition without altering the methodological point. Our aim here is to introduce the indirect double-differencing scheme and to establish its feasibility on a single, well-defined instrument pair (OLI-2 against

https://doi.org/10.5194/egusphere-2026-2803
Preprint. Discussion started: 18 June 2026

MSI). Having done so, the same framework can be applied without modification to other sensors including Sentinel-2C or Landsat-8 OLI which we leave to future work.

This last point sets the natural direction for future work. The methodology developed here is general: any sufficiently stable, hyperspectral instrument with a non-Sun-synchronous (or pointable) orbit can play the role currently played by EMIT. The proposed SI-traceable satellite (SITSat) missions – in particular CLARREO Pathfinder (Roithmayr et al., 2014) and TRUTHS (Fox and Green, 2020) – are explicitly designed to provide on-orbit radiometric calibration traceable to SI standards, and would substantially reduce the dominant uncertainty contribution of the present scheme by replacing the few-percent radiometric uncertainty of EMIT with sub-percent SI-traceable values. Substituting either of these missions for EMIT in the double-differencing framework would deliver simultaneously absolute calibration and cross-mission alignment between Landsat-9 and Sentinel-2, providing a robust foundation for the long-term, harmonised land-surface records that motivate combined use of the two missions in the first place. In practical terms, the percent-level offsets identified above set a useful target for the harmonisation algorithms underpinning operational products such as HLS, and provide a global, scene-diverse cross-check that complements site-based assessments of L9–S2 interoperability.

Code and data availability. The Landsat-9 OLI-2, Sentinel-2 MSI, and EMIT Level-1 products used in this study are publicly available through the Google Earth Engine (GEE) data catalogue (Gorelick et al., 2017), under the collection identifiers `LANDSAT/LC09/C02/T1_TOA`, `COPERNICUS/S2_HARMONIZED`, and `NASA/EMIT/L1B/RAD`, respectively. We additionally considered the dataset `COPERNICUS/S2_CLOUD_PROBABILITY` for Sentinel-2 cloud probability. All processing was performed within the GEE platform. The analysis scripts developed for this work are available from the authors upon request.

Author contributions. JG developed the research concept and contributed to the analysis and coding support. FB developed the code and produced the results. Both authors contributed to writing and reviewing the manuscript.

Competing interests. The contact author has declared that none of the authors has any competing interests

Acknowledgements. This research received no external funding.

https://doi.org/10.5194/egusphere-2026-2803
Preprint. Discussion started: 18 June 2026

References

Bouvet, M., Thome, K., Berthelot, B., Bialek, A., Czapla-Myers, J., Fox, N., Goryl, P., Henry, P., Ma, L., Marcq, S., Meygret, A., Wenny, B., and Woolliams, E.: RadCalNet: A Radiometric Calibration Network for Earth Observing Imagers Operating in the Visible to Shortwave Infrared Spectral Range, Remote Sensing, 11, https://doi.org/10.3390/rs11202401, 2019.

Chance, K. and Kurucz, R.: An improved high-resolution solar reference spectrum for earth's atmosphere measurements in the ultraviolet, visible, and near infrared, Journal of Quantitative Spectroscopy and Radiative Transfer, 111, 1289–1295, https://doi.org/https://doi.org/10.1016/j.jqsrt.2010.01.036, special Issue Dedicated to Laurence S. Rothman on the Occasion of his 70th Birthday., 2010.

Chander, G., Markham, B. L., and Helder, D. L.: Summary of current radiometric calibration coefficients for Landsat MSS, TM, ETM+, and EO-1 ALI sensors, Remote Sensing of Environment, 113, 893–903, https://doi.org/10.1016/j.rse.2009.01.007, 2009.

Chander, G., Hewison, T. J., Fox, N., Wu, X., Xiong, X., and Blackwell, W. J.: Overview of Intercalibration of Satellite Instruments, IEEE Transactions on Geoscience and Remote Sensing, 51, 1056–1080, https://doi.org/10.1109/TGRS.2012.2228654, 2013a.

Chander, G., Mishra, N., Helder, D. L., Aaron, D. B., Angal, A., Choi, T., Xiong, X., and Doelling, D. R.: Applications of Spectral Band Adjustment Factors (SBAF) for Cross-Calibration, IEEE Transactions on Geoscience and Remote Sensing, 51, 1267–1281, https://doi.org/10.1109/TGRS.2012.2228141, 2013b.

Coleman, R. W., Thompson, D. R., Brodrick, P. G., Ben Dor, E., Cox, E., Pérez García-Pando, C., Hoefen, T., Kokaly, R. F., Meyer, J. M., Ochoa, F., Okin, G. S., Heller Pearlshtien, D., Swayze, G., and Green, R. O.: An accuracy assessment of the surface reflectance product from the EMIT imaging spectrometer, Remote Sensing of Environment, 315, 114 450, https://doi.org/10.1016/j.rse.2024.114450, 2024.

Coluzzi, R., Imbrenda, V., Lanfredi, M., and Simoniello, T.: A first assessment of the Sentinel-2 Level 1-C cloud mask product to support informed surface analyses, Remote Sensing of Environment, 217, 426–443, https://doi.org/https://doi.org/10.1016/j.rse.2018.08.009, 2018.

Drusch, M., Del Bello, U., Carlier, S., Colin, O., Fernandez, V., Gascon, F., Hoersch, B., Isola, C., Laberinti, P., Martimort, P., Meygret, A., Spoto, F., Sy, O., Marchese, F., and Bargellini, P.: Sentinel-2: ESA's optical high-resolution mission for GMES operational services, Remote Sensing of Environment, 120, 25–36, https://doi.org/10.1016/j.rse.2011.11.026, 2012.

Farhad, M. M., Kaewmanee, M., Leigh, L., and Helder, D.: Radiometric Cross Calibration and Validation Using 4 Angle BRDF Model between Landsat 8 and Sentinel 2A, Remote Sensing, 12, https://doi.org/10.3390/rs12050806, 2020.

Fox, N. and Green, P.: Traceable Radiometry Underpinning Terrestrial- and Helio-Studies (TRUTHS): An Element of a Space-Based Climate and Calibration Observatory, Remote Sensing, 12, https://doi.org/10.3390/rs12152400, 2020.

Gascon, F., Bouzinac, C., Thépaut, O., Jung, M., Francesconi, B., Louis, J., Lonjou, V., Lafrance, B., Massera, S., Gaudel-Vacaresse, A., Languille, F., Alhammoud, B., Viallefont, F., Pflug, B., Bieniarz, J., Clerc, S., Pessiot, L., Trémas, T., Cadau, E., De Bonis, R., Isola, C., Martimort, P., and Fernandez, V.: Copernicus Sentinel-2A Calibration and Products Validation Status, Remote Sensing, 9, https://doi.org/10.3390/rs9060584, 2017.

Gorelick, N., Hancher, M., Dixon, M., Ilyushchenko, S., Thau, D., and Moore, R.: Google Earth Engine: Planetary-scale geospatial analysis for everyone, Remote Sensing of Environment, 202, 18–27, https://doi.org/10.1016/j.rse.2017.06.031, big Remotely Sensed Data: tools, applications and experiences, 2017.

https://doi.org/10.5194/egusphere-2026-2803
Preprint. Discussion started: 18 June 2026

Gorroño, J., Banks, A. C., Fox, N. P., and Underwood, C.: Radiometric inter-sensor cross-calibration uncertainty using a traceable high accuracy reference hyperspectral imager, ISPRS Journal of Photogrammetry and Remote Sensing, 130, 393–417, https://doi.org/https://doi.org/10.1016/j.isprsjprs.2017.07.002, 2017.

Gorroño, J., Solé, M. P., Fox, N., Guanter, L., August, T., and Fehr, T.: Global Assessment of Directional Effects in the Intercalibration of Optical Satellite Instruments With the TRUTHS Mission, IEEE Transactions on Geoscience and Remote Sensing, 62, 1–13, https://doi.org/10.1109/TGRS.2024.3483969, 2024.

Green, R. O., Mahowald, N., Ung, C., Thompson, D. R., Bator, L., Bennet, M., Bernas, M., Blackway, N., Bradley, C., Cha, J., Clark, P., Clark, R., Cloud, D., Diaz, E., Ben Dor, E., Duren, R., Eastwood, M. L., Ehlmann, B. L., Fuentes, L., Ginoux, P., et al.: The Earth Surface Mineral Dust Source Investigation: An Earth Science Imaging Spectroscopy Mission, in: 2020 IEEE Aerospace Conference, pp. 1–15, https://doi.org/10.1109/AERO47225.2020.9172731, 2020.

Helder, D., Markham, B., Morfitt, R., Storey, J., Barsi, J., Gascon, F., Clerc, S., LaFrance, B., Masek, J., Roy, D. P., Lewis, A., and Pahlevan, N.: Observations and Recommendations for the Calibration of Landsat 8 OLI and Sentinel 2 MSI for Improved Data Interoperability, Remote Sensing, 10, https://doi.org/10.3390/rs10091340, 2018.

Helder, D. L., Basnet, B., and Morstad, D. L.: Absolute radiometric calibration of Landsat using a pseudo invariant calibration site, IEEE Transactions on Geoscience and Remote Sensing, 51, 1360–1369, https://doi.org/10.1109/TGRS.2013.2243738, 2013.

JCGM: Evaluation of measurement data - Guide to the expression of uncertainty in measurement, Tech. Rep. 100, 2008.

Jing, X., Leigh, L., Pinto, C. T., and Helder, D.: Evaluation of RadCalNet Output Data Using Landsat 7, Landsat 8, Sentinel 2A, and Sentinel 2B Sensors, Remote Sensing, 11, 541, https://doi.org/10.3390/rs11050541, 2019.

Ju, J., Zhou, Q., Freitag, B., Roy, D. P., Zhang, H. K., Sridhar, M., Mandel, J., Arab, S., Schmidt, G., Crawford, C. J., Gascon, F., Strobl, P. A., Masek, J. G., and Neigh, C. S.: The Harmonized Landsat and Sentinel-2 version 2.0 surface reflectance dataset, Remote Sensing of Environment, 324, 114 723, https://doi.org/https://doi.org/10.1016/j.rse.2025.114723, 2025.

Levy, R., Miller, J. A., Barsi, J. A., Thome, K. J., and Markham, B. L.: Landsat 9 Transfer to Orbit of Pre-Launch Absolute Calibration of Operational Land Imager (OLI), Remote Sensing, 16, https://doi.org/10.3390/rs16081360, 2024.

Markham, B., Barsi, J., Kvaran, G., Ong, L., Kaita, E., Biggar, S., Czapla-Myers, J., Mishra, N., and Helder, D.: Landsat-8 Operational Land Imager Radiometric Calibration and Stability, Remote Sensing, 6, 12 275–12 308, https://doi.org/10.3390/rs61212275, 2014.

Masek, J., Wulder, M., Markham, B., McCorkel, J., Crawford, C., Storey, J., and Jenstrom, D.: Landsat 9: Empowering open science and applications through continuity, Remote Sensing of Environment, 248, 111 968, https://doi.org/10.1016/j.rse.2020.111968, 2020.

Mishra, N., Helder, D., Angal, A., Choi, J., and Xiong, X.: Absolute Calibration of Optical Satellite Sensors Using Libya 4 Pseudo Invariant Calibration Site, Remote Sensing, 6, 1327–1346, https://doi.org/10.3390/rs6021327, 2014.

Pelletier, F., Cardille, J. A., Wulder, M. A., White, J. C., and Hermosilla, T.: Inter- and intra-year forest change detection and monitoring of aboveground biomass dynamics using Sentinel-2 and Landsat, Remote Sensing of Environment, 301, 113 931, https://doi.org/https://doi.org/10.1016/j.rse.2023.113931, 2024.

Pinto, C. T., Ponzoni, F. J., Castro, R. M., Leigh, L., Kaewmanee, M., Aaron, D., and Helder, D.: Evaluation of the uncertainty in the spectral band adjustment factor (SBAF) for cross-calibration using Monte Carlo simulation, Remote Sensing Letters, 7, 837–846, https://doi.org/10.1080/2150704X.2016.1190474, 2016.

Roger, J., Guanter, L., and Gorroño, J.: Assessing the Detection of Methane Plumes in Offshore Areas Using High-Resolution Imaging Spectrometers, Atmospheric Measurement Techniques, 18, 5545–5567, https://doi.org/10.5194/amt-18-5545-2025, 2025.

https://doi.org/10.5194/egusphere-2026-2803
Preprint. Discussion started: 18 June 2026

Roithmayr, C. M., Lukashin, C., Speth, P. W., Kopp, G., Thome, K., Wielicki, B. A., and Young, D. F.: CLARREO Approach for Reference Intercalibration of Reflected Solar Sensors: On-Orbit Data Matching and Sampling, IEEE Transactions on Geoscience and Remote Sensing, 52, 6762–6774, https://doi.org/10.1109/TGRS.2014.2302397, 2014.

Shrestha, M., Sampath, A., Kim, M., and Park, S.: System characterization report on the Earth Surface Mineral Dust Source Investigation (EMIT) sensor, in: System characterization of Earth observation sensors, edited by Ramaseri Chandra, S. N., no. 2021–1030 in Open-File Report, pp. 1–27, U.S. Geological Survey, https://doi.org/10.3133/ofr20211030R, chapter R, 2024.

Sinergise and Amazon Web Services: Sentinel-2 on AWS, https://registry.opendata.aws/sentinel-2/, 2024.

Stedman, M., Hunt, S. E., De Vis, P., Bantges, R., Brindley, H., and Fox, N.: Impact of Characterization on Cross-Calibration Performance for Multispectral Sensors With SI-Traceable Satellite Mission TRUTHS, IEEE Transactions on Geoscience and Remote Sensing, 63, 1–16, https://doi.org/10.1109/TGRS.2025.3633954, 2025.

Tan, W., He, H., Chen, X., and Qi, W.: Analyzing the influence of atmosphere on optical remote sensing in 400 to 2500 nm wavelength spectrum, in: AOPC 2020: Optical Spectroscopy and Imaging; and Biomedical Optics, edited by Liu, J., Wang, Y., Ling, Z., Sun, Y., and Jin, D., vol. 11566, p. 115660I, International Society for Optics and Photonics, SPIE, https://doi.org/10.1117/12.2579576, 2020.

Thompson, D. R., Green, R. O., Bradley, C., Brodrick, P. G., Mahowald, N., Ben Dor, E., Bennett, M., Bernas, M., Carmon, N., Chadwick, K. D., Clark, R. N., Coleman, R. W., Cox, E., Diaz, E., Eastwood, M. L., Eckert, R., Ehlmann, B. L., Ginoux, P., Gonçalves Ageitos, M., Grant, K., Guanter, L., Heller Pearlshtien, D., Helmlinger, M., Herzog, H., Hoefen, T., Huang, Y., Keebler, A., Kalashnikova, O., Keymeulen, D., Kokaly, R., Klose, M., Li, L., Lundeen, S. R., Meyer, J., Middleton, E., Miller, R. L., Mouroulis, P., Oaida, B., Obiso, V., Ochoa, F., Olson-Duvall, W., Okin, G. S., Painter, T. H., Pérez García-Pando, C., Pollock, R., Realmuto, V., Shaw, L., Sullivan, P., Swayze, G., Thingvold, E., Thorpe, A. K., Vannan, S., Villarreal, C., Ung, C., Wilson, D. W., and Zandbergen, S.: On-orbit calibration and performance of the EMIT imaging spectrometer, Remote Sensing of Environment, 303, 113 986, https://doi.org/10.1016/j.rse.2023.113986, 2024.

Thuillier, G., Hersé, M., Labs, D., Foujols, T., Peetermans, W., Gillotay, D., Simon, P., and Mandel, H.: The Solar Spectral Irradiance from 200 to 2400 nm as Measured by the SOLSPEC Spectrometer from the Atlas and Eureca Missions, Solar Physics, 214, 1–22, https://doi.org/10.1023/A:1024048429145, 2003.

Xu, L., Herold, M., Tsendbazar, N.-E., Masiliūnas, D., Li, L., Lesiv, M., Fritz, S., and Verbesselt, J.: Time series analysis for global land cover change monitoring: A comparison across sensors, Remote Sensing of Environment, 271, 112 905, https://doi.org/https://doi.org/10.1016/j.rse.2022.112905, 2022.

Zhang, H. K., Roy, D. P., Yan, L., Li, Z., Huang, H., Vermote, E., Skakun, S., and Roger, J.-C.: Characterization of Sentinel-2A and Landsat-8 top of atmosphere, surface, and nadir BRDF adjusted reflectance and NDVI differences, Remote Sensing of Environment, 215, 482–494, https://doi.org/https://doi.org/10.1016/j.rse.2018.04.031, 2018.